4 Design methodologies of AVAIs for a pneumatic rock drill handle

4.1 Introduction

In this chapter the design methodologies of two AVAIs will be described. These methodologies will concentrate on the design requirements of a handle for a pneumatic rock drill. Many of the more practical aspects of the design of these devices are application-specific, but the basic requirement of coincidence of the excitation and isolation frequencies is universal as is the method of achieving coincidence. The rock drill design is particularly demanding because the input contains significant amplitudes at frequencies other than the impact frequency. Furthermore, the low overall mass and size required as well as cost and robustness are necessary constraints.

This chapter will start with a discussion of the effects of tool vibration on the operators of hand-held machinery. Current strategies for the reduction of hand tool vibration will be reviewed. It will then continue with measurements that were done for a specific drill that is in widespread operation in South African gold mines. These measurements were done to assess the current exposure of operators to vibration and will be used as the baseline for any reduction method. The design methodologies used for the two handles will then be discussed and evaluated. Here the problems related to noise in the input will be addressed as well as the many practical aspects particular to each design.

4.2 Vibration reduction of tool handles

Exposure of the fingers and hands to long periods of shock or vibration can lead to a number of disorders threatening the operators of hand-held tools with irreversible damage. Five disorders are described by Griffen (1998) and are listed in Table 4.1. Combinations of these disorders are referred to as Hand-Arm Vibration Syndrome (HAVS). The disorder that has received the most attention from researchers is the vascular disorder Vibration White Finger (VWF). VWF is characterised by the occasional whitening (blanching) of the fingertips especially when exposed to a cold environment. Attacks are often accompanied by numbness and tingling and in rare cases gangrene has been reported. VWF is also associated with primary Raynaud's disease, which is a hereditary disease not caused by vibration. Currently there is no treatment for the disease and prevention is therefore essential, which means that workers must be reassigned as soon as symptoms are noticed.

Table 4.1: Disorders associated with HAVS

Type	Disorder
A	Circulatory
B	Bone and joint
C	Neurological
D	Muscle
E	General (e.g. central nervous system)

Due to the debilitating effect of VWF it has been classified as an industrial disease in 1985 in the United Kingdom (Raw, 1999). In 1999 the UK government agreed to pay £500 million to 30 000 former coal mine workers suffering from the disease. In South Africa there has been concern that the widespread use of pneumatic drills in underground mining operations can lead to similar personal suffering and claims. A comprehensive study of vibration levels of several different rock drills used in South African mines measured an average weighted equivalent acceleration of 24 m/s^2 in underground operation (Van Niekerk, Heyns & Heyns, 2000). The Commission of European Communities' proposed directive on physical agents (1994) prescribes an action level of weighted 8-hour equivalent acceleration ($a_{h,w(eq,8h)}$) of 2.5 m/s^2 and a threshold value of 5 m/s^2. The 8-hour value is calculated using the time exposed to the high levels as a ratio of an 8-hour workday. Short duration vibration can therefore be higher than the stated values, but there are absolute limits of 10 and 20 m/s^2 corresponding to the action and threshold values as illustrated in Figure 4.1. The action level involves measures to reduce the vibration while the threshold value is an absolute limit where work must be stopped.

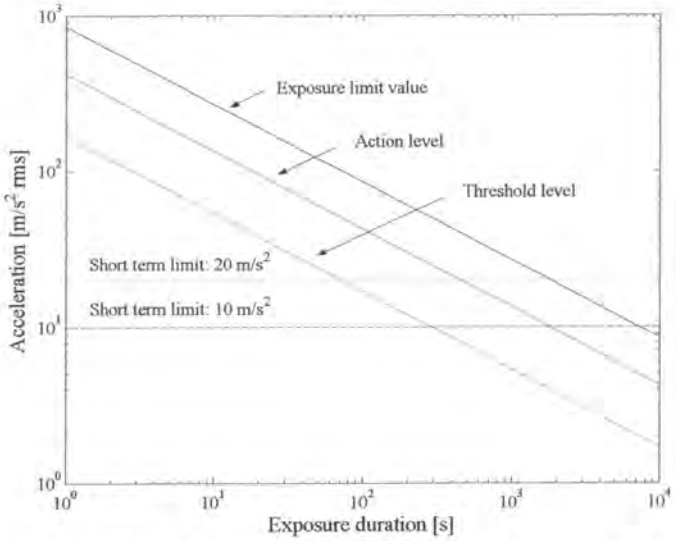

Figure 4.1: Threshold level, action level and exposure limit of the proposed EU directive on physical agents

There are two options available to meet these criteria namely, limiting exposure time or reducing the vibration level. Since the weighted equivalent acceleration of pneumatic drills used in South African mines are already above the short-term value the only option is the latter.

The standard pneumatic drill handle is shown in Figure 4.2(a). No isolation is provided and the steel handle is simply bolted to the back end of the drill. Simple solutions such as elastomeric handle wraps and gloves have been shown to have negligible isolation effect. This is because they isolate at high frequencies, typically larger than 250 Hz, where the hand is less sensitive to damage. Gloves are sometimes recommended because they keep the hands warm, which may lessen the damage (Griffen, 1998).

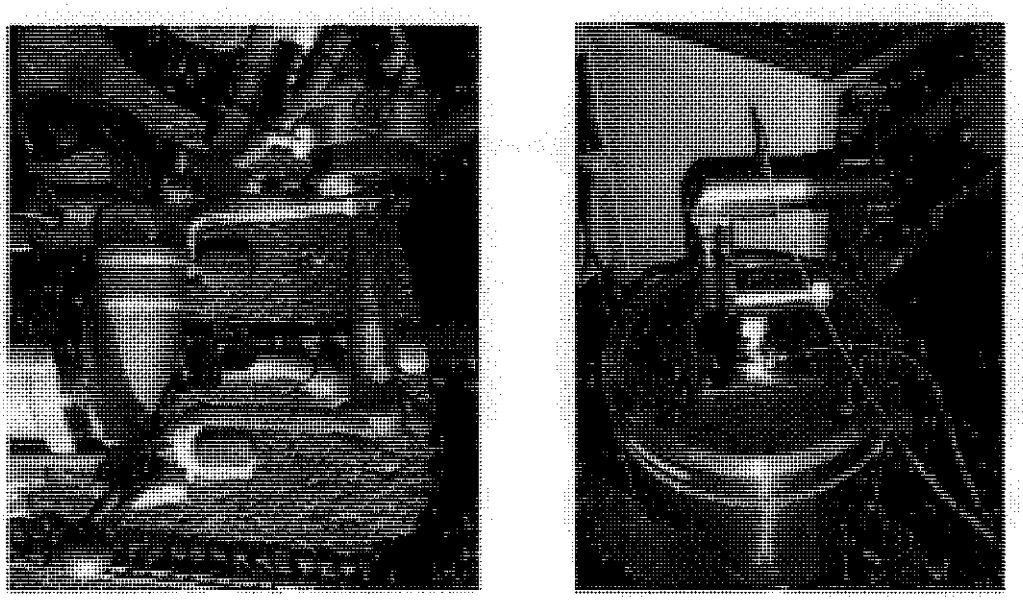

(a) (b)

Figure 4.2: (a) Standard handle, (b) isolated handle in transmissibility test set-up

If an operator is expected to drill continuously for 8-hours the vibration levels must be limited to 10% of the current value, which will be a considerable achievement. A proposed isolated handle is shown in Figure 4.2(b). The development of this handle is described by Prajapati and Hes (1999). The main problem with using isolators in this application is that a low natural frequency is directly in conflict with the static deflection requirement. A low static deflection is necessary for the operator to remain in control of the tool. The natural frequency is related to the static deflection:

$$\omega_n = \sqrt{\frac{F}{m\delta_{st}}} \tag{4.1}$$

where δ_{st} is the static deflection, F the thrust force of the operator and m the combined mass of the handle and the operator's hand. The displacement transmissibility for an undamped system at the excitation frequency (ω_e) is (Chapter 1):

$$\frac{X}{Y} = \frac{1}{1-\left(\frac{\omega_e}{\omega_n}\right)^2} \tag{4.2}$$

For a 10% transmissibility the excitation frequency ratio must be 3.2. For a pneumatic drill with an operating frequency of 35 Hz the required natural frequency will be 11 Hz. According to Griffin (1990) the apparent mass of the hand at 35 Hz is ~0.4 kg. The handle mass was measured as 1.745 kg and the total sprung mass is therefore 2.145 kg. For a thrust force of 150 N the static deflection will be ~15 mm. Such a large deflection will not be acceptable for safe tool use. Often preload of the spring is used to limit the deflection experienced by the operator. In this case the preload was measured to be ~12 kg. The only problem with using preload is that it is difficult to be certain that the operator always pushes with the same force.

Other solutions have been reported, for instance, Alabuzhev *et al.* (1989) suggested vibration reduction using quasi-zero stiffness handles on jackhammers and riveting tools. Barber (1992) also reported other methods, which required fundamental design changes to the machine to reduce the vibration experienced by the operator. Palej *et al.* (1993) showed that an active pneumatic spring could have a dynamic stiffness 20 times lower than its static stiffness and subsequently reduced vibration of a riveter 4 times. Raw (1999) achieved a 45% vibration reduction on a road-breaking tool by using a lead-silicone composite material to cover its handle, each suspended lead particle essentially acting as a vibration absorber. Andersson (1990) showed an 85% reduction in acceleration for a hammer drill using an isolated handle. Bisutti (2001) showed that the addition of mass could greatly reduce the vibration of hand tools. In his design water is pumped from a storage tank to the tool at the moment it is switched on and back when switched off. This addition of mass achieved a 60% reduction of handle vibration. Gwinn and Marjoram (1999) describes several isolated handle concepts. The first shown in Figure 4.3 uses a softening spring as the isolation element (annotation 44A). The purpose of the softening spring is to provide a lower spring rate at the operating point after the application of the thrust force by the operator. The moment put on the handle is transferred using a bearing (annotation 40A and 40B). In Figure 4.4 a vibration absorber is put in the load path forming a VAI. The mass of the absorber is shown as annotation 86. Figure 4.5 describes a handle with a fixed frequency LIVE type isolator, similar to the one proposed in this thesis. The design is greatly complicated by the air supply that runs through the handle. This necessitates a seal, in this case two O-rings (annotation 84), which will add considerable amounts of damping to the system.

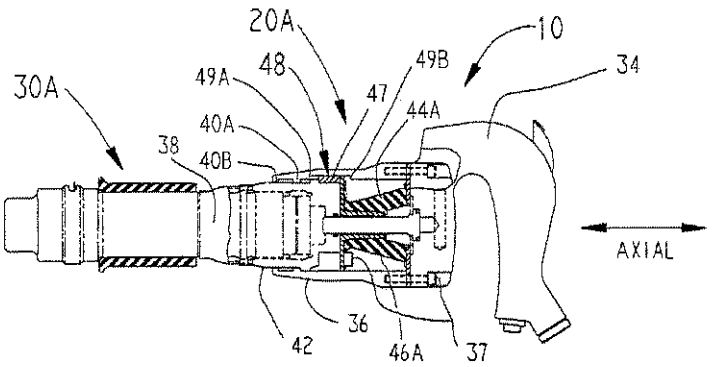

Figure 4.3: Isolated handle (Gwinn & Marjoram, 1999)

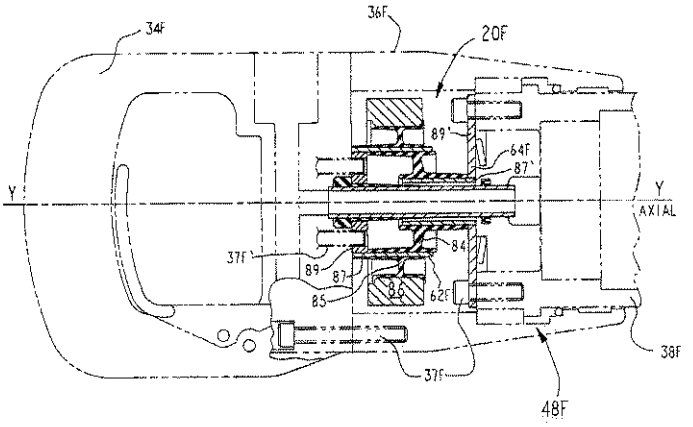

Figure 4.4: Handle with VAI (Gwinn & Marjoram, 1999)

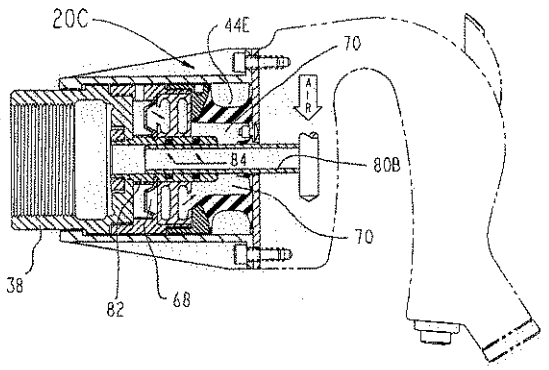

Figure 4.5: Handle with AVAI (Gwinn & Marjoram, 1999)

It is important to note that the pneumatic rock drill's operation differs from most other pneumatic tools in that the forward thrust is provided by a pneumatic piston called a jack-leg. The operator is required to counterbalance the vertical force and normally does this by leaning on the handle with his right hand, while his left hand is used to operate the jack-leg pressure control valve (Figure 4.6). It seems therefore that it will be important for the handle to be able to transfer this moment to the drill, while the axial stiffness is less important. Some axial stiffness is, however, still necessary since the drill is often jerked to remove the drill steel from the face. A minimum stiffness of 100 N/mm should be sufficient since it will allow a static deflection of 3 mm at a force of 30 kg.

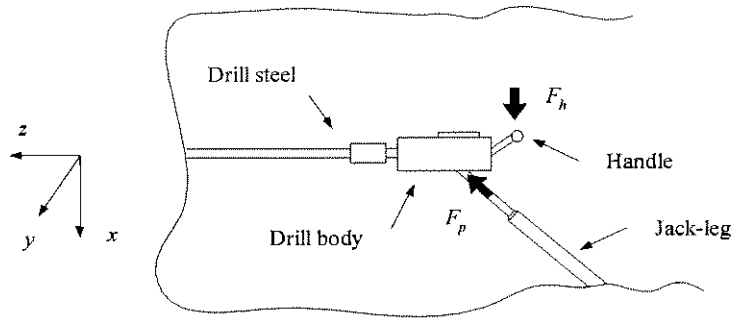

Figure 4.6: Pneumatic rock drill operation

4.3 Vibration measurement of a Boart Longyear S250 pneumatic rock drill

At the start of this work the standard regarding measurement and assessment of hand transmitted vibration was ISO 5349:1986. The measurements were done using the guidelines in this standard. ISO 5349:2001 was published in June 2001 and differs from the previous standard in many respects. The most important difference is that the evaluation of the weighted rms acceleration is done in vector fashion, while previously only the dominant axis was used. The experimental work followed the procedure of the earlier standard and to allow for continuity the theoretical part will be developed using the same standard. In the following paragraphs the assessment procedure will be described

specifically for the current drill handle. Later the response of the new handle will be compared to this reference design to show the improvement that is possible.

The measurement set-up is shown in Figure 4.7 and Figure 4.8. The drill is a percussive tool with the z-direction the axis of operation. The x-direction is vertical and the y-direction horizontal. Three Brüel & Kjær type 4393 charge accelerometers were used to measure the operational vibration of the handle. The accelerometers were mounted on mechanical filters with a cut-off frequency of 3000 Hz in accordance with the standard's guideline for percussive tools. The handle did not have any additional isolation material (Figure 4.2a) and is usually used with a work glove that offers negligible isolation. The pressure was also measured to establish the relationship between excitation frequency and supply pressure. It was additionally found that the pressure measurement could be used to calculate the excitation frequency. Such an approach could be much cheaper than using a piezoelectric accelerometer.

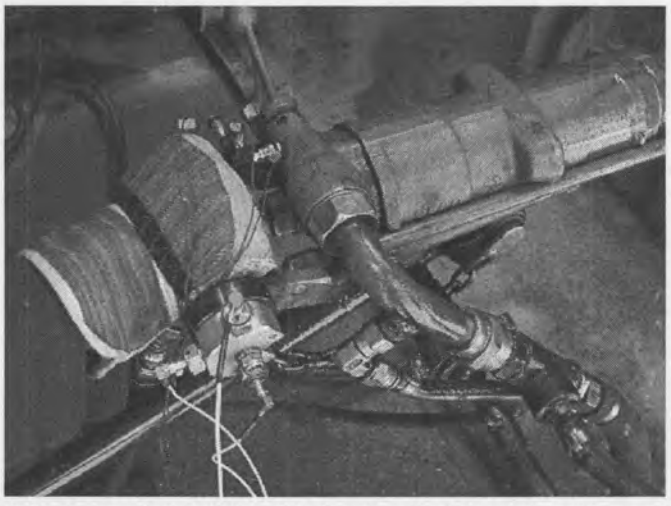

Figure 4.7: Instrumented drill handle showing the tri-axial accelerometer set-up

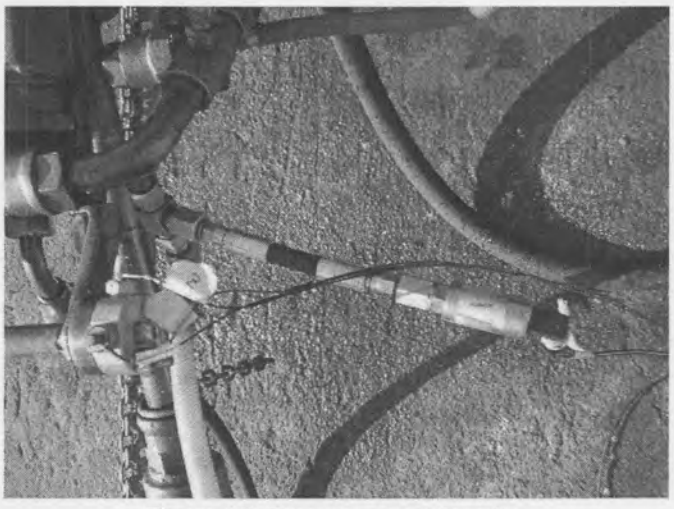

Figure 4.8: Pressure sensor location

The test started with a collaring operation shown in Figure 4.9. The collaring establishes a starting hole for the drilling operation. After collaring the second operator lets go of the drill steel and the drilling commences. The memory of the Siglab 20-42 FFT analyser allowed for 32 seconds of data to be sampled at 5120 Hz on 4 channels. The specified frequency range of 5-1500 Hz is easily covered. This corresponded to an almost complete hole of ~1.8 m at the maximum pressure tested. At lower pressure the drill speed is lower. Because the drill performance is different in different types of rock a standard Norite block is used for all testing. Four drills were measured. Three of these were new and their operational characteristics will probably vary with time. The fourth was a drill used for development work and consequently well run in.

Figure 4.9: Collaring operation

As would be expected the acceleration in the *z*-direction was the largest, but in the other two directions significant values were measured which could have an impact on the design under the new ISO standard. A typical measurement is shown in Figure 4.10. The acceleration values have been integrated to show the handle velocity and displacement. Although 95% of the displacement amplitudes were less than 2 mm for all operating conditions, the absorber has to be able to cope with maximum values of up to 8 mm.

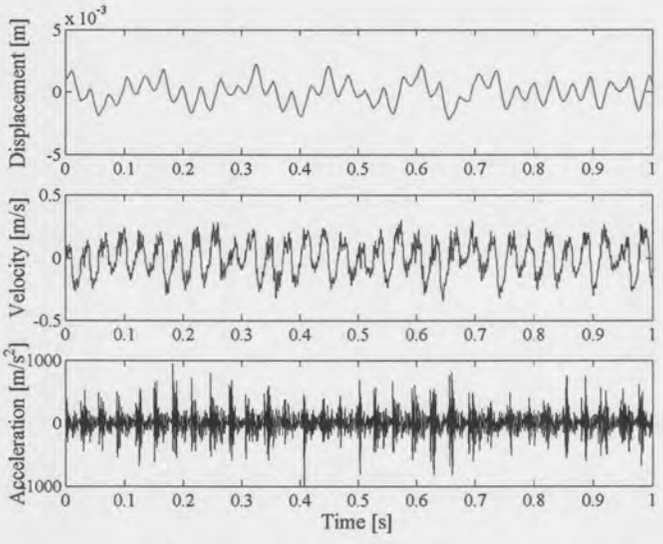

Figure 4.10: Typical measurement in the *z*-direction

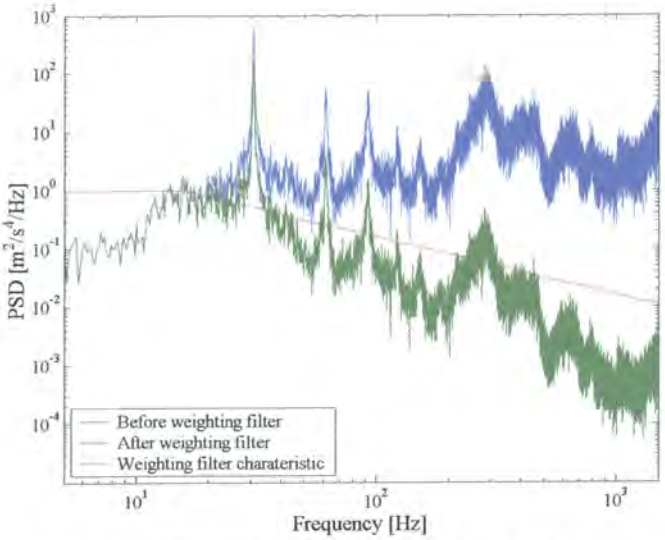

Figure 4.11: Typical PSD of the acceleration in the *z*-direction before and after the application of the weighting filter (Δf = 0.125 Hz, 4 averages)

A typical Power Spectral Density (PSD) of the acceleration is shown in Figure 4.11. The frequency of the impact dominates the spectrum. The large values at frequencies above the excitation frequency is not very important since current evidence indicates that the hand is less sensitive to vibration injury at these frequencies. The weighting curve corresponding to the hand's sensitivity is also shown in the figure. Frequencies below 16 Hz have a weighting of 1. The weighted acceleration can be found by using the relationship:

$$a_{h,w}(f) = a(f)|H(f)| \tag{4.3}$$

where $a_{h,w}(f)$ is the weighted acceleration and $a(f)$ the unweighted acceleration and $H(f)$ the weighting filter characteristic. The rms value of the Fourier transform can be calculated using Parseval's formula (Mead, 2000):

$$a_{h,w} = \sqrt{c_0^2 + \frac{1}{2}\sum_{n=1}^{\infty}|c_n|^2} \tag{4.4}$$

where c_n is the complex Fourier coefficient:

$$c_n = \frac{2}{T}\int_0^T a(t)e^{-in\omega_0 t}dt \tag{4.5}$$

Alternatively the power spectral density of the acceleration can be used:

$$a_{h,w} = \sqrt{\int_0^{\infty} W_a(f)|H(f)|^2 df} \tag{4.6}$$

where $W_a(f)$ is the one-sided power spectral density. In the time domain the rms acceleration can be calculated using a set of digital ⅓ octave band filters.

The weighting is done using:

$$a_{h,w} = \sqrt{\sum_{j=1}^{n} \left(K_j a_{h,j}\right)^2} \tag{4.7}$$

where K_j is the j^{th} ⅓ octave band weighting factor and $a_{h,j}$ is the rms acceleration measured in the j^{th} ⅓ octave band. The ISO 5349:2001 specification prescribes a weighting filter that can be used in the time domain without using ⅓ octave band analysis, which is easier to use and more accurate. Any of the above frequency-domain or time-domain methods can be used, but the narrow-band methods will be more accurate since the approximate nature of the octave band analysis is eliminated.

The test procedure for each drill involved increasing the supply pressure from 300 to 600 kPa in increments of 50 kPa. At each pressure 32 seconds of data were recorded for each of the four drills. Although the weighted rms acceleration values varied widely, the variation in frequency covered the same band between 28.75 and 37.5 Hz for all the drills. This is important if the handle is to be mass-produced. The weighted acceleration for the various supply pressures is shown in Table 4.2. The excitation frequency can be estimated using a transformation to the frequency domain such as a PSD or a Fourier transform and picking the maximum value or by using zero crossings in the time domain. Zero crossings of a band-pass filtered displacement signal will be faster for similar accuracy than a frequency-domain method.

Table 4.2: Comparison of weighted acceleration and frequency band values of the four drills

Drill	Weighted acceleration [m/s^2]		Excitation frequency [Hz]	
	Minimum	Maximum	Minimum	Maximum
1	10.51	18.16	30.625	36.250
2	9.38	13.37	30.000	36.875
3	8.91	17.28	28.750	37.500
4	8.28	18.72	28.750	37.500

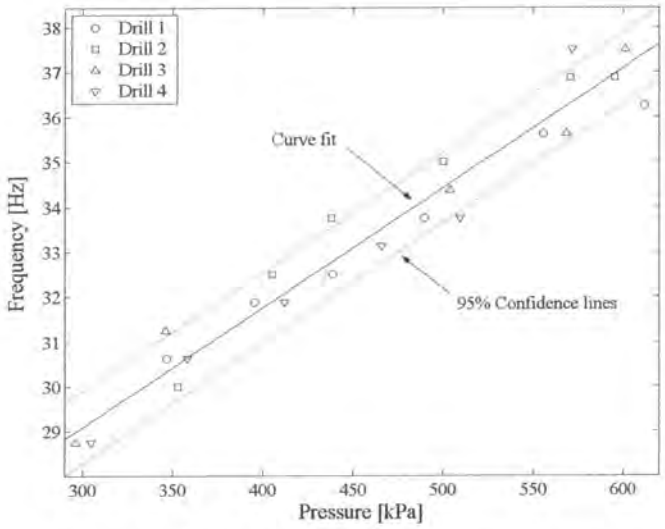

Figure 4.12: Curve fit of frequency *vs.* pressure values

When the excitation frequency *vs.* pressure is plotted a clear trend emerges as shown in Figure 4.12. As the supply pressure increases, the excitation frequency increases linearly. Since four machines where tested of which one was well run in there is reason to believe that well-maintained machines will fall within the 95% confidence lines. If the handle is designed so that the bandwidth enveloped the excitation frequencies, then good performance for any drill can be ensured. The main innovation of the AVAI as applied to the handle lies in the fact that the stiffness of the air spring can be made to be a function of the supply line air pressure and therefore it will be self-tuning. This is a major advantage in an environment where the use of an electronic control system will be expensive.

4.4 Type I amplified vibration-absorbing isolator

This section will document the design of the type I AVAI. Firstly, from measured data it was clear that the excitation does not consist of a single frequency and that the effect of noise in the input must be assessed. The following paragraph will analyse the effect of noise in the input. Subsequently, the insight gained from the general approach will be used to simulate the exact handle response using the measured input.

4.4.1 Narrow-band excitation with noise

As shown in §4.3 the excitation consists of large magnitude excitation over a limited frequency band as well as low and high frequency noise and harmonics. In general excitation of this type can be enveloped as shown in Figure 4.13. For the following discussion the AVAI response will be calculated in a non-dimensional sense in order to preserve generality. Firstly, it is assumed that the average of the narrow-band excitation ($\tilde{\omega}_e$) is half of the total bandwidth ($\Delta\Omega_e$). This assumption is done simply to illustrate the effect of noise and bandwidth and does not directly pertain to the handle excitation.

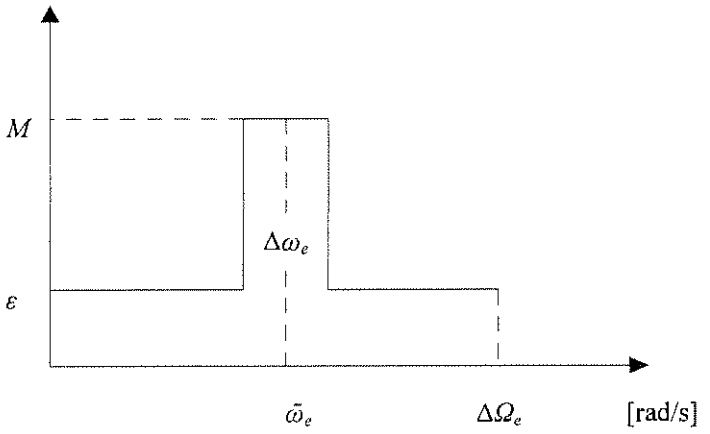

Figure 4.13: Power spectral density envelope

The following two non-dimensional ratios can now be defined. The ratio of noise (ε) to peak magnitude (M) is:

$$n = \frac{\varepsilon}{M} \tag{4.8}$$

The ratio of excitation bandwidth ($\Delta\omega_e$) to noise bandwidth ($\Delta\Omega_e$):

$$B = \frac{\Delta\omega_e}{\Delta\Omega_e} \tag{4.9}$$

The one-sided PSD of the response is:

$$W_x(i\omega) = W_y(i\omega)\left|H(i\omega)\right|^2 \tag{4.10}$$

where x describes the response and y the input and H is the transfer function of the isolator. The mean square of the response can be calculated in the frequency domain (Rao, 1990):

$$\bar{X} = \int_0^{\Delta\Omega_e} W_x(i\omega)\,d\omega = \int_0^{\Delta\Omega_e} W_y(i\omega)\left|H(i\omega)\right|^2 d\omega \tag{4.11}$$

The ratio of output to input mean square response is:

$$\bar{R} = \frac{\bar{X}}{\bar{Y}} = \frac{\int_0^{\Delta\Omega_e} W_y(i\omega)\left|H(i\omega)\right|^2 d\omega}{\int_0^{\Delta\Omega_e} W_y(i\omega)\,d\omega} \tag{4.12}$$

The numerator of Equation (4.12) can be expanded as follows:

$$\begin{aligned}\int_0^{\Delta\Omega_e} W_y(i\omega)\left|H(i\omega)\right|^2 d\omega = {} & \int_0^{\Delta\Omega_e/2-\Delta\omega_e/2} W_y(i\omega)\left|H(i\omega)\right|^2 d\omega + \int_{\Delta\Omega_e/2-\Delta\omega_e/2}^{\Delta\Omega_e/2+\Delta\omega_e/2} W_y(i\omega)\left|H(i\omega)\right|^2 d\omega \\ & + \int_{\Delta\Omega_e/2+\Delta\omega_e/2}^{\Delta\Omega_e} W_y(i\omega)\left|H(i\omega)\right|^2 d\omega\end{aligned} \tag{4.13}$$

Integrating by parts for one of the terms in Equation (4.13) gives:

$$\begin{aligned}\int_0^{\Delta\Omega_e/2-\Delta\omega_e/2} W_y(i\omega)\left|H(i\omega)\right|^2 d\omega = {} & W_y(i\omega)\Big|_0^{\Delta\Omega_e/2-\Delta\omega_e/2} \int_0^{\Delta\Omega_e/2-\Delta\omega_e/2}\left|H(i\omega)\right|^2 d\omega \\ & - \int_0^{\Delta\Omega_e/2-\Delta\omega_e/2} \frac{dW_y(i\omega)}{d\omega}\left(\int_0^{\Delta\Omega_e/2-\Delta\omega_e/2}\left|H(i\omega)\right|^2 d\omega\right)d\omega \\ \text{but}\quad \frac{dW_y(i\omega)}{d\omega} = 0 & \\ \therefore\quad \int_0^{\Delta\Omega_e/2-\Delta\omega_e/2} W_y(i\omega)\left|H(i\omega)\right|^2 d\omega = {} & W_y(i\omega)\Big|_0^{\Delta\Omega_e/2-\Delta\omega_e/2} \int_0^{\Delta\Omega_e/2-\Delta\omega_e/2}\left|H(i\omega)\right|^2 d\omega\end{aligned} \tag{4.14}$$

The total response is now:

$$\begin{aligned}\int_0^{\Delta\Omega_e} W_y(i\omega)\left|H(i\omega)\right|^2 d\omega = {} & W_y(i\omega)\Big|_0^{\Delta\Omega_e/2-\Delta\omega_e/2} \int_0^{\Delta\Omega_e/2-\Delta\omega_e/2}\left|H(i\omega)\right|^2 d\omega \\ & + W_y(i\omega)\Big|_{\Delta\Omega_e/2-\Delta\omega_e/2}^{\Delta\Omega_e/2+\Delta\omega_e/2} \int_{\Delta\Omega_e/2-\Delta\omega/2}^{\Delta\Omega_e/2+\Delta\omega/2}\left|H(i\omega)\right|^2 d\omega + W_y(i\omega)\Big|_{\Delta\Omega_e/2+\Delta\omega_e/2}^{\Delta\Omega_e} \int_{\Delta\Omega_e/2+\Delta\omega_e/2}^{\Delta\Omega_e}\left|H(i\omega)\right|^2 d\omega\end{aligned} \tag{4.15}$$

Solving for the input described in Figure 4.13:

$$\int_0^{\Delta\Omega_e} W_y(i\omega)\,d\omega = 2\varepsilon\left(\Delta\Omega_e - \Delta\omega_e\right) + M\Delta\omega_e \tag{4.16}$$

The ratio ($\bar{R}$) of output ($\bar{X}$) to input ($\bar{Y}$) mean square response is now:

$$\bar{R} = \frac{\frac{\varepsilon}{M}\int_0^{\Delta\Omega_e/2-\Delta\omega_e/2}\left|H(i\omega)\right|^2 d\omega + \int_{\Delta\Omega_e/2-\Delta\omega_e/2}^{\Delta\Omega_e/2+\Delta\omega_e/2}\left|H(i\omega)\right|^2 d\omega + \frac{\varepsilon}{M}\int_{\Delta\Omega_e/2+\Delta\omega_e/2}^{\Delta\Omega_e}\left|H(i\omega)\right|^2 d\omega}{2\frac{\varepsilon}{M}\left(\Delta\Omega_e - \Delta\omega_e\right) + \Delta\omega_e} \tag{4.17}$$

When the AVAI is compared to a single degree of freedom isolator the result is:

$$\frac{\bar{R}_{AVAI}}{\bar{R}_{SDOF}} = \frac{\frac{\varepsilon}{M}\int_0^{\Delta\Omega_e/2-\Delta\omega_e/2}\left|H_{AVAI}(i\omega)\right|^2 d\omega + \int_{\Delta\Omega_e/2-\Delta\omega_e/2}^{\Delta\Omega_e/2+\Delta\omega_e/2}\left|H_{AVAI}(i\omega)\right|^2 d\omega + \frac{\varepsilon}{M}\int_{\Delta\Omega_e/2+\Delta\omega_e/2}^{\Delta\Omega_e}\left|H_{AVAI}(i\omega)\right|^2 d\omega}{\frac{\varepsilon}{M}\int_0^{\Delta\Omega_e/2-\Delta\omega_e/2}\left|H_{SDOF}(i\omega)\right|^2 d\omega + \int_{\Delta\Omega_e/2-\Delta\omega_e/2}^{\Delta\Omega_e/2+\Delta\omega_e/2}\left|H_{SDOF}(i\omega)\right|^2 d\omega + \frac{\varepsilon}{M}\int_{\Delta\Omega_e/2+\Delta\omega_e/2}^{\Delta\Omega_e}\left|H_{SDOF}(i\omega)\right|^2 d\omega} \quad (4.18)$$

Since for the type I AVAI the first natural frequency is constant, this frequency will be used for comparison with a conventional isolator. The transmissibility for an isolator was given in Chapter 1. The parameters used for the comparison are summarised in Table 4.3. The values were chosen to allow comparison of the methods and to draw general conclusions as to the suitability of the AVAI for this type of excitation.

Table 4.3: Values used for the comparison

Description	Parameter	Value
Centre frequency of excitation	$\bar{\omega}_e$	10
Noise bandwidth	$\Delta\Omega_e$	20
Mass ratio	m_b/m_y	0.003
Area ratio	A_b/A_a	5
Second damping ratio	$\bar{\zeta}_2$	0.01
Stiffness ratio	μ_k	0.36...0.4

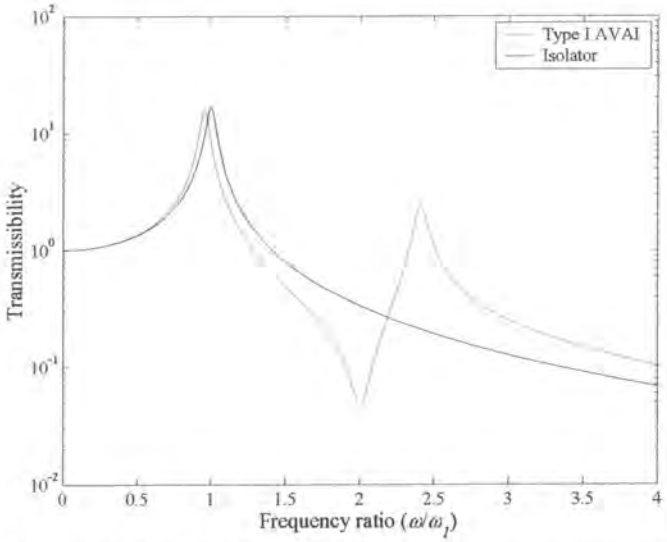

Figure 4.14: Type I AVAI and isolator used in the comparison

The two transmissibilities that are compared are shown in Figure 4.14. Clearly, for an undamped case the mean square response will be infinite due to the infinite response at the natural frequencies. It can also immediately be seen that the isolator will provide the best isolation if the bandwidth of the noise is infinite.

The ratio of ratios ($\bar{R}_{AVAI}/\bar{R}_{SDOF}$ in Equation (4.18)) is a measure of the benefit of the AVAI over an isolator and can be plotted as a function of three of the non-dimensional ratios namely damping,

excitation bandwidth ratio and noise ratio. One of the non-dimensional ratios must be held constant while the other two are being varied to create a contour plot showing the combination of variables that create an advantage for the AVAI. In Figure 4.15 through Figure 4.17 it can be seen that there is a benefit for the AVAI at small excitation bandwidth ratios (blue region), while at large excitation bandwidth ratios there is an advantage for the isolator (red region). This is not unexpected since the AVAI has been shown to be effective over a very limited bandwidth. It is interesting to note that for each excitation bandwidth ratio an optimal damping value exists. For a practical application where the noise floor and excitation bandwidth ratio are known, the optimal damping ratio can therefore be read from such a graph. It can also be seen that the optimal damping ratio is lower for the same excitation bandwidth ratio as the noise ratio is reduced. This is also not unexpected since the introduction of damping will reduce the response at the natural frequency (which will be infinite at zero damping) and even small noise ratios will therefore dominate the response. Figure 4.18 through Figure 4.20 show the effect of reducing the noise ratio if the excitation bandwidth ratio is fixed. The first two figures show similar trends i.e. some damping is necessary even at low noise ratios and the required damping increases as the noise ratio is increased. The last graph shows that a large excitation bandwidth ratio cannot be corrected using damping and an AVAI is therefore inappropriate in such a case.

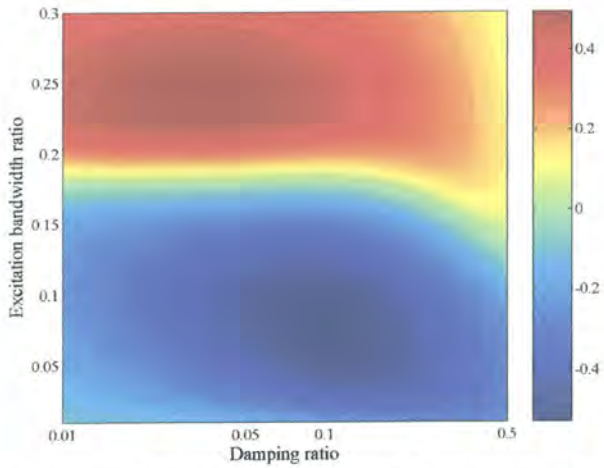

Figure 4.15: The logarithm of the ratio of ratios for a case with noise ratio 10^{-3}

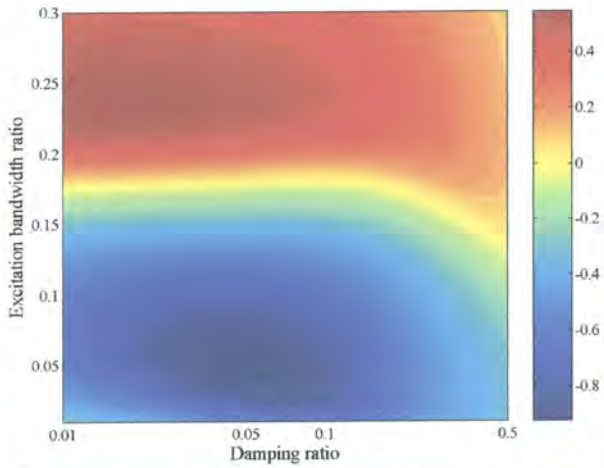

Figure 4.16: The logarithm of the ratio of ratios for a case with noise ratio 10^{-4}

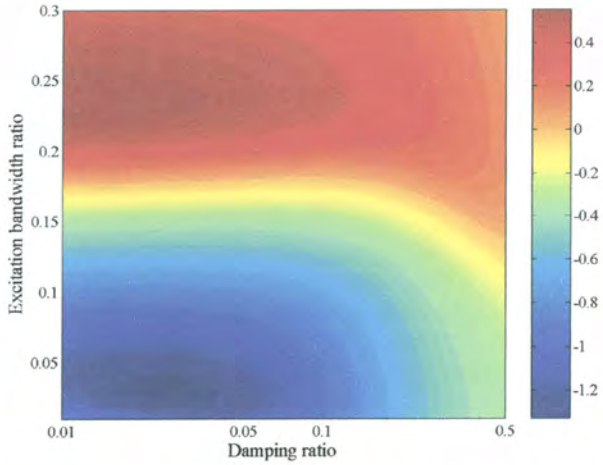

Figure 4.17: The logarithm of the ratio of ratios for a case with noise ratio 10^{-5}

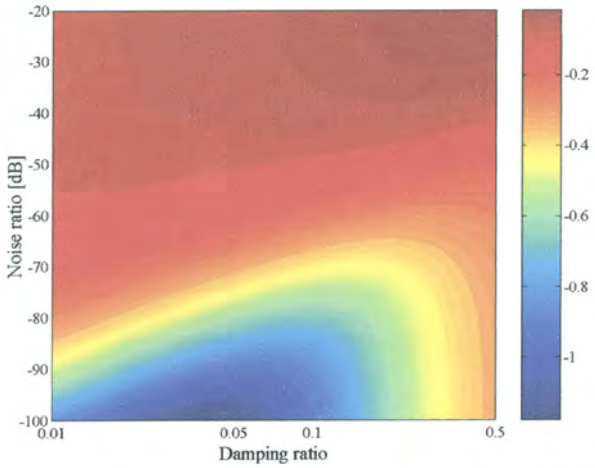

Figure 4.18: The logarithm of the ratio of ratios for a case with excitation bandwidth ratio 0.01

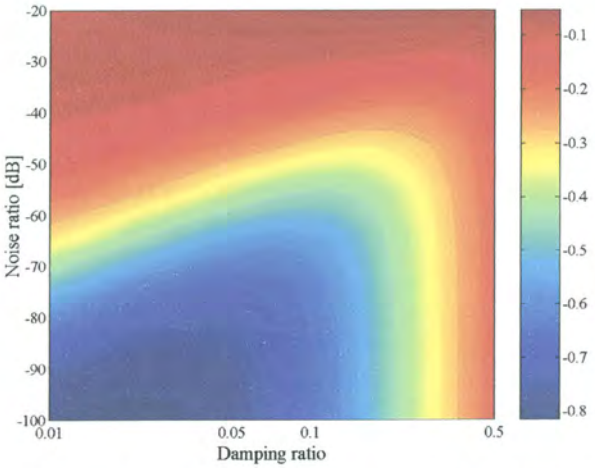

Figure 4.19: The logarithm of the ratio of ratios for a case with excitation bandwidth ratio 0.1

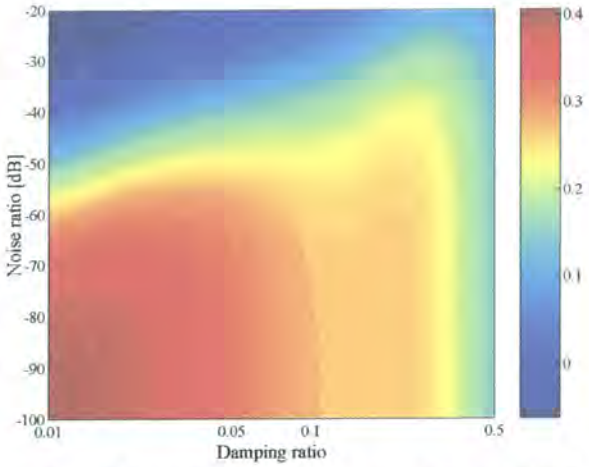

Figure 4.20: The logarithm of the ratio of ratios for a case with excitation bandwidth ratio 0.2

Figure 4.15 through Figure 4.20 show that an optimal value of damping exists for each noise and excitation bandwidth ratio. It seems as if a damping specification should enter the design as an additional parameter to those considered in Chapter 2. However, it will be very difficult to realise in a practical device. Inevitably some damping will be present, which can only be removed with the addition of energy as discussed in Chapter 1. If damping needs to be added, this can easily be done in a device that uses fluid in the port by obstructing the flow (for instance with the addition of a variable pitch butterfly valve in the port). The controllable addition of damping will be more difficult for a slug type device. For a type I device it could be possible to make both the damping and stiffness variable so that the optimal values for both will always be guaranteed. For the present work the design will attempt to reduce the damping as much as possible so that the addition of damping or variable damping can easily be considered in future work. The main sources of flow-related damping are the entrance and exit losses of the port as well as friction in the port. Careful design can reduce these losses. Overall damping is, however, dominated by the elastomeric material of the spring that is used, which can be minimised by choosing a low damping material.

4.4.2 Type I AVAI design

The design is shown schematically in Figure 4.21. The normal design approach for LIVE type isolators as well as vibration absorbers is to build devices and then to tune each before it is used. For absorbers this is often done by adding or subtracting mass. For a LIVE type isolator this can be done by sleeving the port. The purpose of the present design is to characterise the influence of assumptions made during the design. If the absorber can be designed accurately in the first instance, the amount of modification needed can be minimised. The assumptions made will be different for each design, but it could be possible to find design rules for certain classes of devices (i.e. type I), which could then at least give the designer the ability to scale its dimensions.

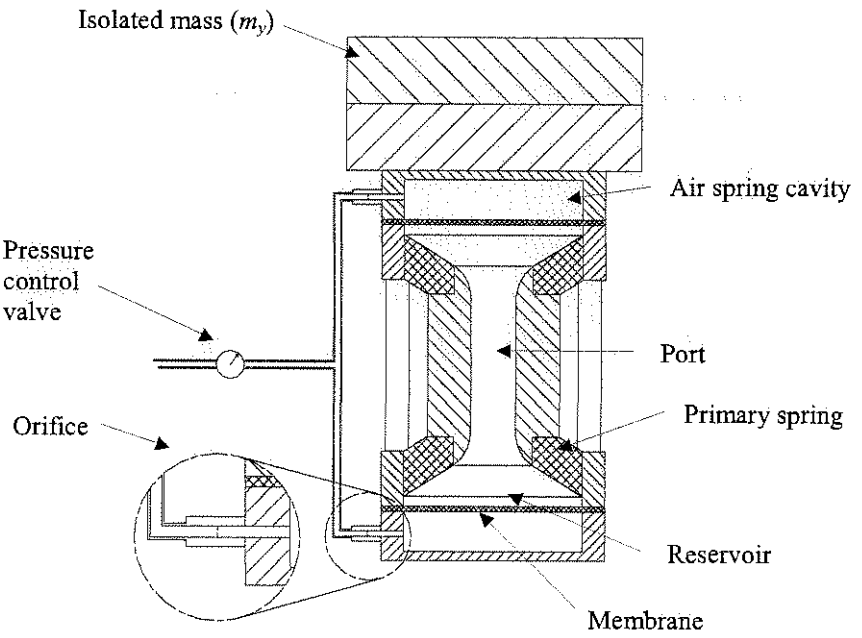

Figure 4.21: Schematic of type I AVAI design

Of all the parameters determining the design the stiffness is the most difficult to estimate accurately. For the type I AVAI the stiffness elements are the primary spring, the membrane stiffness and the stiffness contributed by the air spring. The primary spring stiffness is a function of geometry, boundary conditions and dynamic material properties. The description of dynamic material properties requires extensive testing. As a first estimate static material properties will be used.
The membrane stiffness can be calculated using the pressure deflection equation for a clamped circular plate (Young & Budynas, 2002):

$$k_m = \frac{64\pi E t^3}{3d_b^2\left(1-\nu^2\right)} \tag{4.19}$$

with t the membrane thickness, E the modulus of elasticity and ν the Poisson's ratio. A soft rubber (Nitrile) was used for the membrane of which the maximum Young's modulus was estimated to be less than 20 MPa. For a 2 mm thick rubber membrane the stiffness will be much smaller than that of the air spring.

The air spring stiffness for a closed double-acting air spring is a function of displacement (Figure 4.22) [Equation (D.4)]:

$$k_a(x) = nP_i A_b h^n \left[\left(\frac{1}{h-x}\right)^{n+1} + \left(\frac{1}{h+x}\right)^{n+1}\right]$$

$$\text{for } x \ll h \tag{4.20}$$

$$k_a = \frac{2nP_i A_b}{h}$$

where n is the ratio of specific heats (1.4 for air), P_i the initial air pressure and h the undeflected air spring height.

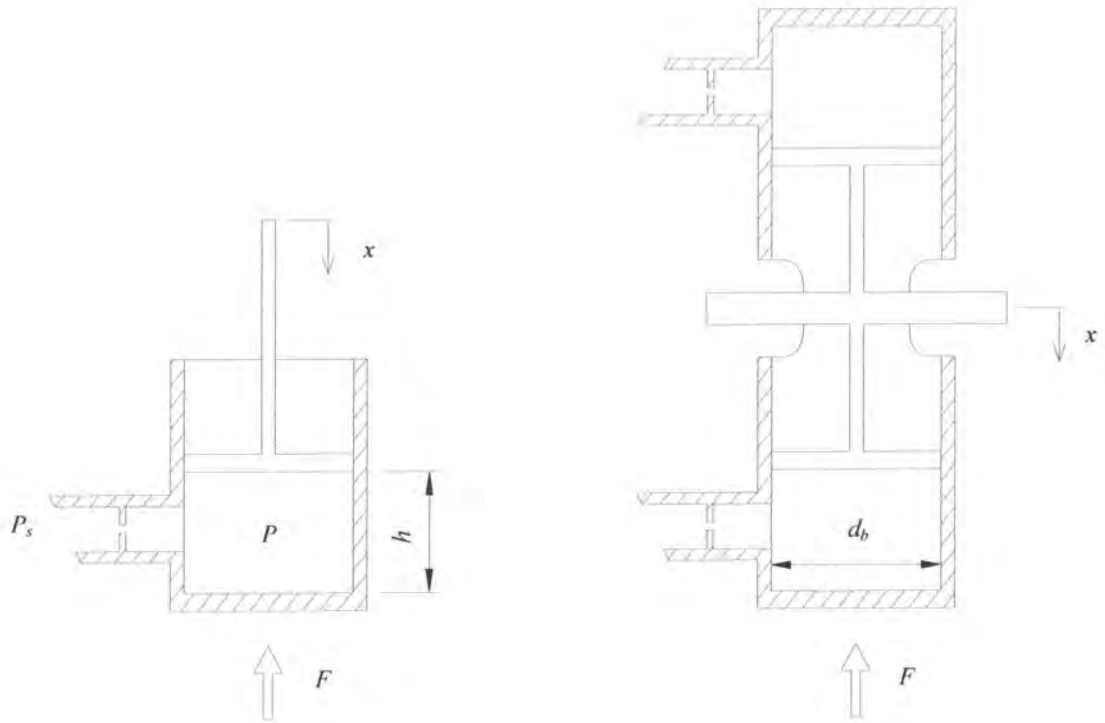

Figure 4.22: Single and double acting air springs

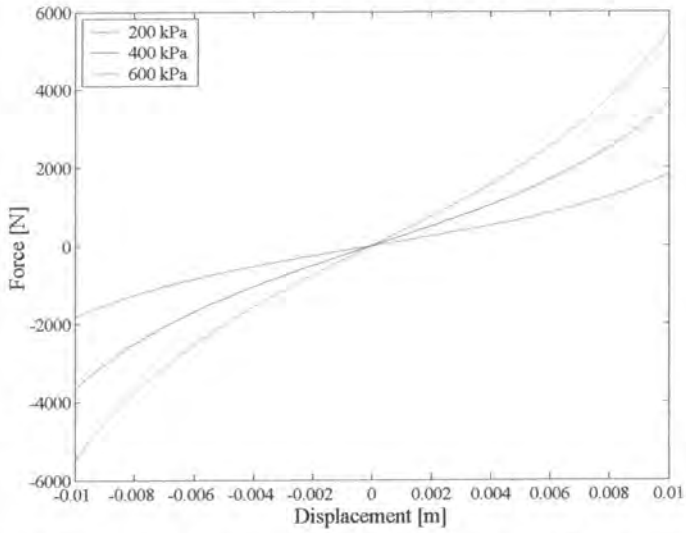

Figure 4.23: Spring force as a function of displacement (h = 20 mm and d_b = 75 mm)

Examination of Equation (4.20) shows that the two practical methods of changing the air spring stiffness are to modify either the pressure or the air spring height. Ting-Kong (1999) investigated a vibration absorber that changed air spring height and Longbottom *et al.* (1987) patented a vibration

absorber that changed the air pressure in the spring using an arrangement of valves. Since the operational frequency of the drill is related to the air pressure, it is proposed that the air spring be connected directly to the supply pressure through a flow restriction. The flow restriction will ensure that the pressure in the spring can rise on compression instead of simply pushing the air back into the supply line, while a change in the supply line pressure will cause the pressure in the spring to equalise after some time delay. This assembly will essentially achieve the same objective as the vibration absorber described by Longbottom *et al.*, without the complexity of a valve arrangement. The disadvantage is a longer time delay in changing the pressure, additional damping and lower stiffness.

Air spring damping is known to be very low, for example, Firestone commercial air spring literature states a damping ratio of 0.03. Damping in an air spring originates from heat transfer and from material losses in the rubber composite bellows. Above 3 Hz the compression process is adiabatic and heat transfer losses will become negligible (Cavanaugh, 1976). In this design the losses through the port is an additional source of damping. These losses can be minimised by using a small orifice. There will be a trade-off between the amount of damping added and the time delay and a decision here will have to take the application considered into account.

Two sets of theory exist that can be used to describe flow in and out of an air spring. Cavanaugh (1976) assumed that the air spring is connected to an auxiliary tank through a capillary, while Palej *et al.* (1993) considered a connection through an orifice. The capillary theory results in algebraic equations, which can easily be solved while the flow through an orifice requires that a non-linear differential equation be solved. A capillary can further be distinguished from an orifice because the flow resistance results from wall friction rather than gas momentum. Although the theory is certainly more complicated, it is much easier to source an orifice and for this design a standard liquid petroleum (LP) gas bottle orifice of 0.15 mm diameter was used.

The mass flow rate through an orifice is given by (Palej *et al.*, 1993):

$$\dot{m} = \begin{cases} CA_0P_s\left\{\dfrac{2n}{n-1}\dfrac{1}{RT_s}\left[\left(\dfrac{P}{P_s}\right)^{2/n} - \left(\dfrac{P}{P_s}\right)^{(n+1)/n}\right]\right\}^{1/2} & \text{for } \sigma_c < \dfrac{P}{P_s} \le 1 \\ CA_0P_s\left[\dfrac{n}{RT_s}\left(\dfrac{2}{n+1}\right)^{(n+1)/(n-1)}\right]^{1/2} & \text{for } 0 \le \dfrac{P}{P_s} \le \sigma_c \end{cases} \tag{4.21}$$

where P_s is the supply pressure, T_s is the absolute supply air temperature, P is the pressure in the spring, R is the gas constant, C the discharge coefficient and A_0 the orifice area. When the pressure in the spring becomes larger than the pressure in the supply line the spring pressure becomes the supply pressure P_s and the supply line the pressure P. In general, the discharge coefficient is a function of the pressure ratio. The product CA_0 is the reduced flow area of the *vena contracta* and the discharge coefficient is therefore always less than 1.

Equation (4.21) can be approximated as follows (Wang & Singh, 1987):

$$\dot{m} = C_c A_0\left[\left|P_s^2 - P^2\right|\frac{1}{RT_s}\right]^{\frac{1}{2}}\operatorname{sign}(P_s - P) \tag{4.22}$$

where C_c is a constant discharge coefficient. A comparison of the two flow rate equations is shown in Figure 4.24. Experimental work by Grace and Lapple (1951) has found that a discharge coefficient of 0.82 is within 2% accurate for an application where the orifice is mounted in a line.

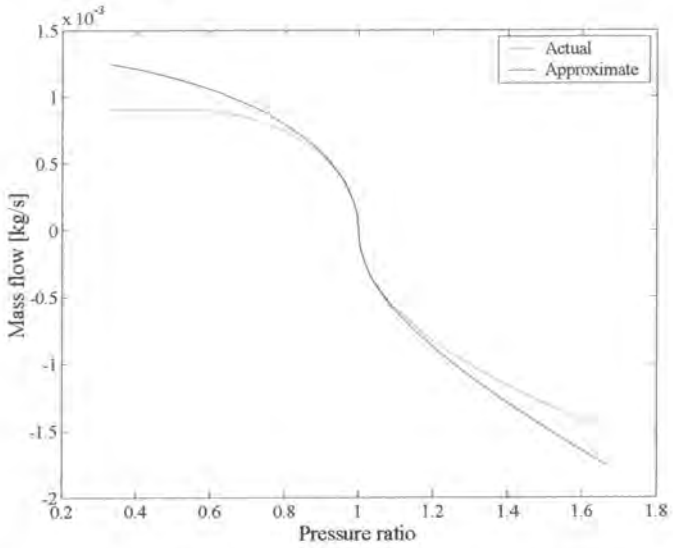

Figure 4.24: Mass flow rate as a function of pressure ratio. The actual curve given by Equation (4.21) and the approximate curve by Equation (4.22) (P_s = 600 kPa, R = 287, T_s = 25°C and C = 0.82)

The differential equation describing the pressure in the air spring is given by (Wang & Singh, 1987):

$$\dot{P} = \frac{1}{V}\left\{ n\dot{m}R\left[\frac{P}{P_0}\right]^{\frac{n-1}{n}} T_0 - nP\dot{V} \right\} \tag{4.23}$$

where P_0 and T_0 are the initial pressure and temperature inside the spring and V is the current volume of air inside the spring. When flow from the spring to the supply line occurs, the gas temperature inside the spring must be used in the mass flow equation. The gas temperature can be found by using the equation for a polytropic thermodynamic process:

$$PT^{n/(1-n)} = P_0 T_0^{n/(1-n)} \tag{4.24}$$

When solving this differential equation the force *vs.* displacement relationship can be calculated for a given displacement input. When the forced displacement is sinusoidal with a constant amplitude and frequency the curve exhibit hysteresis as shown in Figure 4.25. The curve shown is that which is reached after ~50 cycles when the air temperature in the spring has stabilised.

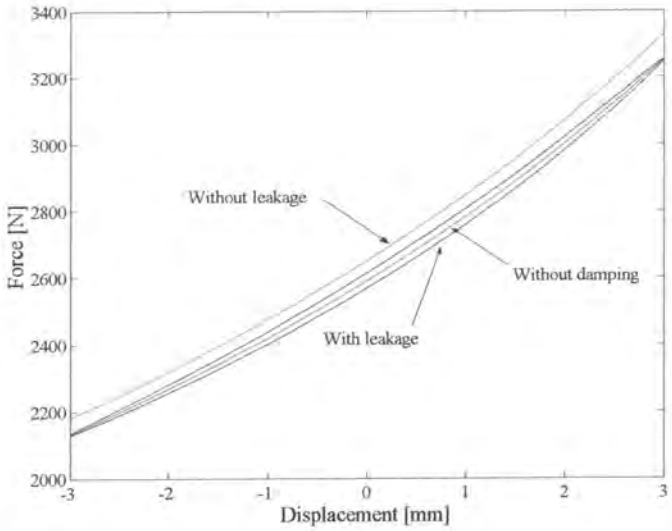

Figure 4.25: Hysteresis curve at 50 Hz compared with an air spring without leakage (d_b = 75 mm, h = 20 mm, X = 3 mm, $T_s = T_0$ = 25°C, P_s = 600 kPa, C = 1 and R = 287 J/kg.K)

The hysteretic damping constant can be calculated by integrating the area bordered by the hysteresis loop (Rao, 1990):

$$h = \frac{\Delta W}{\pi X^2} \tag{4.25}$$

where ΔW is the energy loss during one cycle and X is the excitation amplitude. The loss factor can be found by dividing the hysteretic damping constant by the stiffness. In this case the stiffness is significantly non-linear, but in order to get a basic understanding of the effect of the orifice design on the loss factor it will be assumed to be independent of displacement (i.e. displacement much smaller than the spring height). The effect of orifice diameter is illustrated in Figure 4.26.

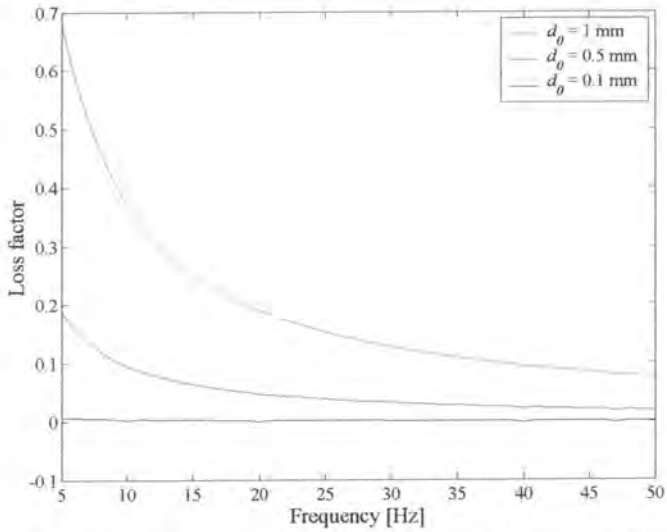

Figure 4.26: Loss factor as a function of frequency and orifice diameter (d_b = 75 mm, h = 20 mm, X = 3 mm, $T_s = T_0$ = 25°C, P_s = 600 kPa, C = 1 and R = 287 J/kg.K)

As would be expected, the loss factor decreases as the orifice diameter decreases. Figure 4.27 shows the effect of orifice diameter on the time taken for the pressure in the air spring to rise to that of the supply line. As would be expected the smaller the diameter, the longer the delay will be. It may also be expected that the air spring will be slightly less stiff than a spring without leakage, as is illustrated in Figure 4.28.

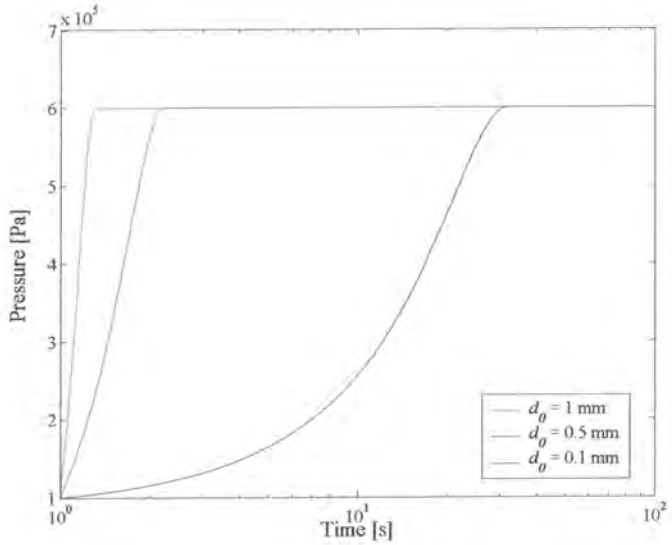

Figure 4.27: Pressure rise from 100 to 600 kPa as a function of orifice diameter d_0 (d_b = 75 mm, h = 20 mm, X = 3 mm, $T_s = T_0$ = 25°C, P_s = 600 kPa, C = 1 and R = 287 J/kg.K)

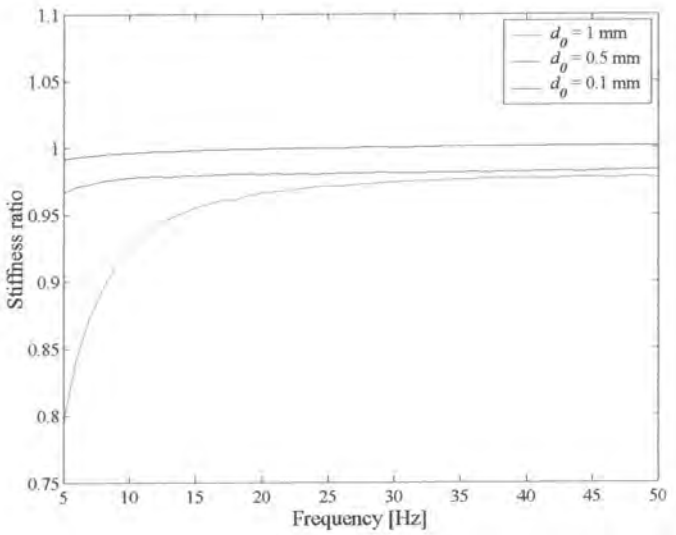

Figure 4.28: Ratio between stiffness of an air spring with and without leakage (d_b = 75 mm, h = 20 mm, X = 3 mm, $T_s = T_0$ = 25°C, P_s = 600 kPa, C = 1 and R = 287 J/kg.K)

Lastly, it is important to keep in mind that up till now the change in volume of the air spring was assumed to be the area multiplied by the displacement, which is not the case for the present design. The air spring volume change is defined by the shape of the membrane and can be written as a function of the displacement of the centre of the membrane (x_c):

$$V = \frac{1}{3} A_b x_c \tag{4.26}$$

The derivation of the displaced volume assumes a fixed boundary for the membrane and is shown in Appendix E.

The primary spring stiffness is a function of the elastomer material property as well as geometry. Time-independent material behaviour for elastomers is generally described in terms of strain energy density functions. The well-known Ogden polynomial model correlates well with experimental data up to 700% strain. Clearly, the maximum strain for the spring will not be that large and it is possible to use linear assumptions to obtain a design value for the stiffness. It is important to keep in mind that elastomers are incompressible and their Poisson's ratio is therefore close to 0.5. The relationship between shear modulus and the modulus of elasticity is:

$$G = \frac{E}{2(1+\nu)} \tag{4.27}$$

The shear modulus is therefore ⅓ of the modulus of elasticity for nearly incompressible materials. As stated before it is required that the stiffness is low and therefore the softest possible low damping rubber will be used. The softest readily available was unfilled natural rubber with hardness 35 Shore A. From Davey and Pane (1964) the modulus of elasticity for his type of rubber can be estimated as ~1.2 MPa.

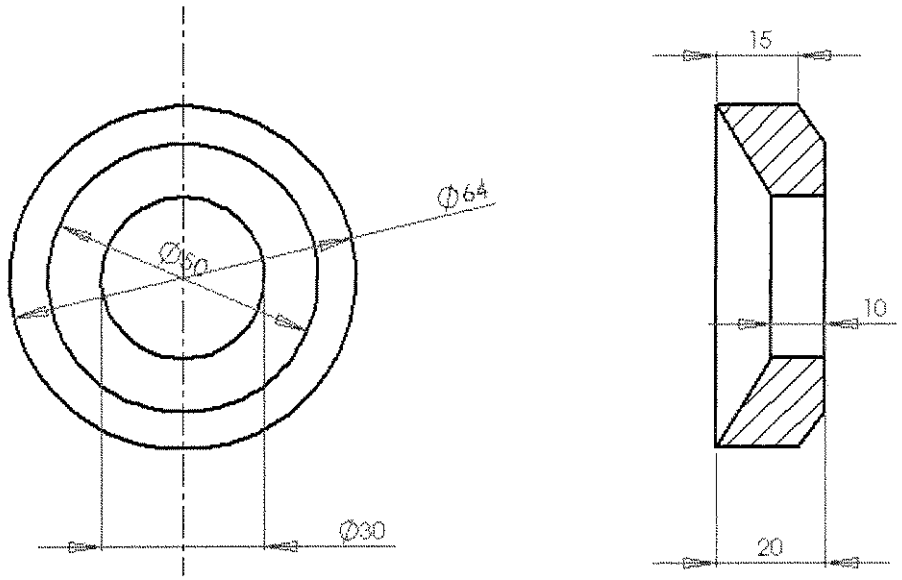

Figure 4.29: Primary spring geometry

The primary spring geometry is shown in Figure 4.29. Due to the boundary condition it will be difficult to find an exact solution for the stiffness. Instead, a number of assumptions will be made and this will be compared with finite element (FE) results to show that they are valid for design purposes. The effect of geometry on the stiffness for a cylindrical spring can be found by summing the stiffness of series springs from the inner to the outer radius (Figure 4.30).

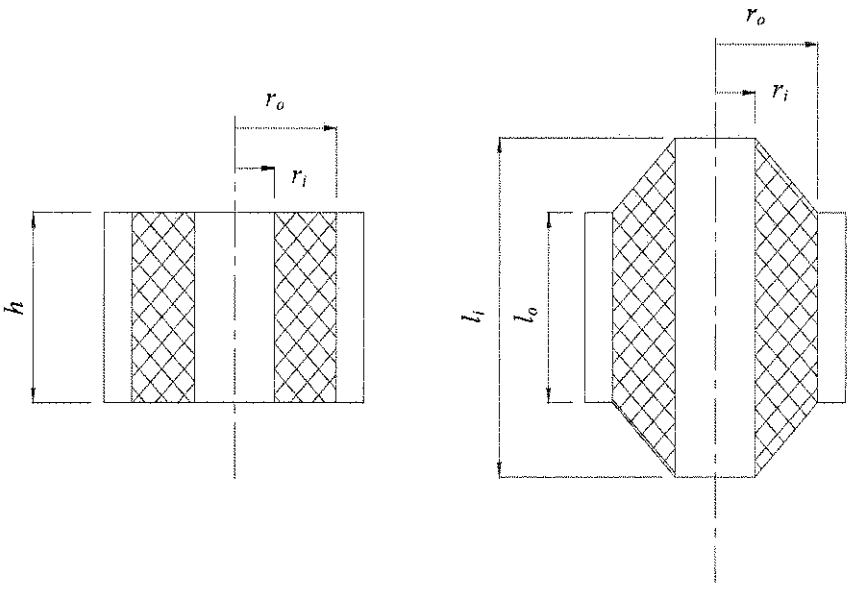

Figure 4.30: Cylindrical spring

A section of the spring at radius r will have a rectangular cross section and assuming that shear effects dominates, the stiffness is (Gere & Timoshenko, 1991):

$$\delta k = \frac{2\pi rhG}{\delta r} \tag{4.28}$$

The total stiffness of the series springs is:

$$\frac{1}{k} = \frac{1}{2\pi G}\int_{r_i}^{r_o}\frac{1}{rh}dr \tag{4.29}$$

If the height is constant the stiffness is:

$$k = \frac{2\pi Gh}{\ln\left(\frac{r_o}{r_i}\right)} \tag{4.30}$$

To separate the effect of the radius ratio from that of material property and height, the geometric stiffness coefficient is defined as:

$$k_{Gh} = \frac{k}{Gh} = \frac{2\pi}{\ln\left(\frac{r_o}{r_i}\right)} \tag{4.31}$$

If the effect of bending is taken into account, the stiffness is given by (Davey & Pane, 1964):

$$k_{Gh} = \frac{k}{Gh} = \frac{1}{\frac{1}{Q_1} + \left(\frac{r_o}{h}\right)^2 \frac{1}{Q_2}} \tag{4.32}$$

where:

$$Q_1 = \frac{2\pi}{\ln\left(\frac{r_o}{r_i}\right)} \tag{4.33}$$

$$Q_2 = \frac{16\pi \left(\frac{r_o}{r_i}\right)^2 \left[\left(\frac{r_o}{r_i}\right)^2 - 1\right]}{3\left\{\left[\left(\frac{r_o}{r_i}\right)^2 - 1\right]^2 - 4\left(\frac{r_o}{r_i}\right)^2 \left[\ln\left(\frac{r_o}{r_i}\right)\right]^2\right\}} \tag{4.34}$$

The geometric stiffness for a tapered section is (Davey & Pane, 1964):

$$k_G = \frac{k}{G} = \frac{2\pi(l_o r_i - l_i r_o)}{(r_o - r_i)\left[\ln(l_o r_i) - \ln(l_i r_o)\right]} \tag{4.35}$$

If the dimensions in Equation (4.35) are chosen such that $l_i r_i = l_o r_o$ then the spring will have uniform shear stress, which can be advantageous. The primary spring stiffness is a function of the ratio of inside and outside diameters as well as the height of the spring, as shown in Figure 4.31. Clearly, for thin sections bending behaviour will dominate and must be accounted for. It must also be kept in mind that thin sections will stretch when the reservoir is pressurised through the motion of the port, which will make the design less efficient. For this reason it is not possible to make a very flexible spring by simply increasing the radius ratio or by decreasing the spring height. A second reason is that the bending stiffness will also decrease significantly, which will make the handle difficult to use in the manner described in §4.2.

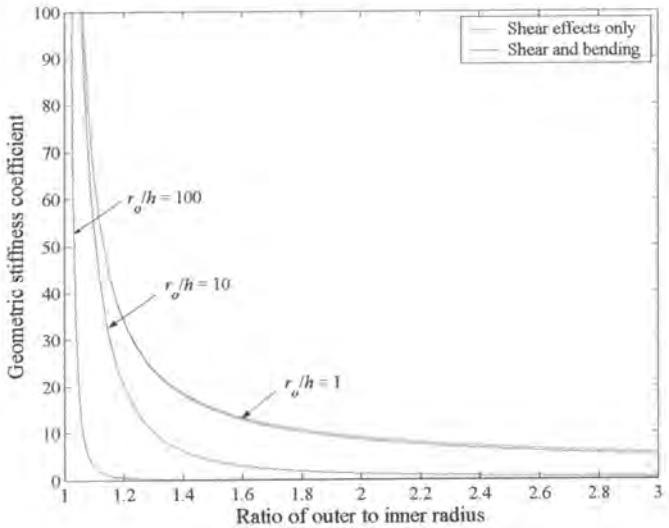

Figure 4.31: Geometric stiffness coefficient

For a general section, as was used in this design, the function describing the height as a function of the radius must be found and then used in Equation (4.29), which can then be integrated numerically. The stiffness can also be found using the exact geometry and the finite element method. For this purpose a finite element model was solved using the MSC.Marc commercial finite element code. The results are summarised in Table 4.4. The compression values were calculated by assuming that the port outer diameter defines the spring inner diameter ($d_i = 2r_i = 50$ mm). This assumption should be valid because the elastomer is incompressible and little deformation will be present past the port outer diameter. In extension it was assumed that the spring inner diameter is defined by the tapered section ($d_i = 30$ mm). The assumptions are confirmed by the finite element analysis shown in Figure 4.32. The extended part shows deformation past the outer diameter of the spring, while in compression there is very little. The force displacement graph as found using finite elements is shown in Figure 4.33. The relationship is fairly linear up to 2 mm, which is adequate since 95% of the measured amplitudes were below 2 mm. This analysis assumes that the material will behave linearly below 2 mm.

Table 4.4: Geometric stiffness using various methods

	Equation	Geometric stiffness (k/G) [m]		
		Extension	Compression	Mean
Exact integration	(4.29)	0.0996	0.3933	0.2465
Rectangular cross section with average height	(4.30)	0.1037	0.3930	0.2483
Rectangular cross section with average height, including bending	(4.32)	0.0723	0.3739	0.2231
Tapered section	(4.35)	0.1285	0.3933	0.2609
Finite element method				0.2969

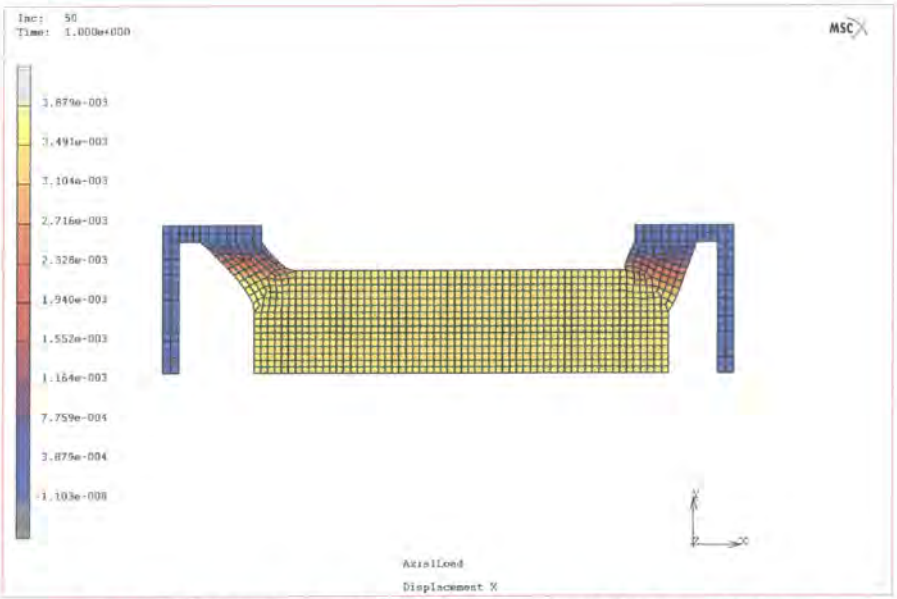

Figure 4.32: Final state of the spring when loaded in the x-direction

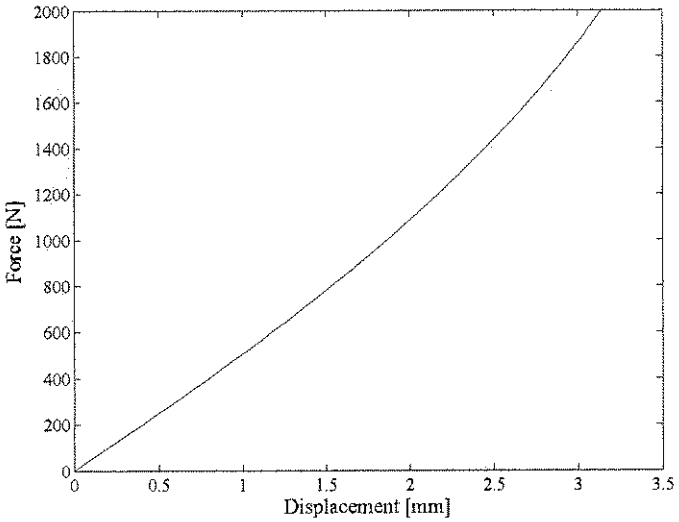

Figure 4.33: Force *vs.* displacement result from the FE model

The effect of a moment acting on the handle is illustrated in Figure 4.34. It is difficult to estimate the amount of angular deflection that will interfere with operator efficiency and comfort. The prudent course of action is to minimise this deflection as much as possible. Appendix D.4 estimates the load required to balance the force of the jack-leg acting on the drill handle. The estimate shows that the load can approach 80 kg, which is comparable to the mass of the operator and is therefore achievable.

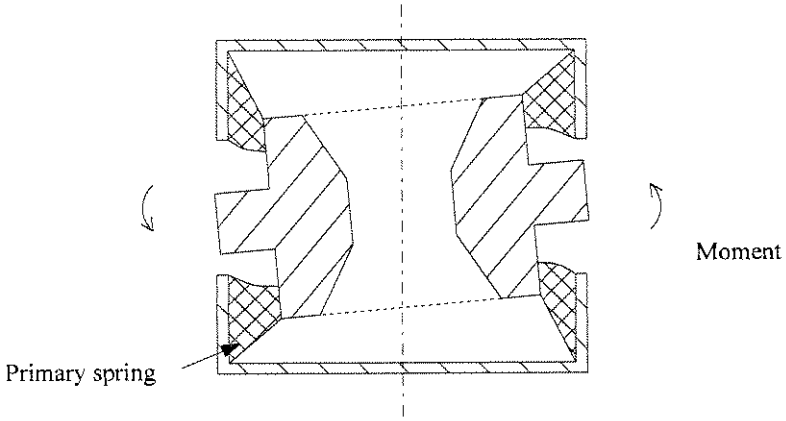

Figure 4.34: Effect of a moment put on the AVAI

The angle through which the handle will rotate can be estimated by calculating the moment balance on the AVAI as shown in Figure 4.35 [Equation (D.11)].

$$\theta = \sin^{-1}\left[\frac{-\frac{F}{k_2}\left(\frac{a}{b}-\frac{1}{2}\right)-\frac{F}{k_1}\left(\frac{a}{b}+\frac{1}{2}\right)}{b}\right] \tag{4.36}$$

For the present design the dimensions are a = 186.76 and b = 105.72 mm.

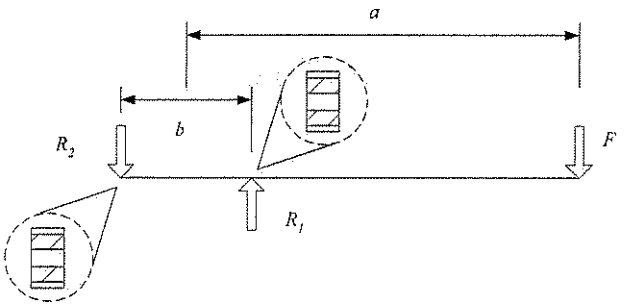

Figure 4.35: Moment acting on the handle

The radial stiffness of the cylindrical spring shown in Figure 4.30 was approximated as follows by Gobel (Davey & Pane, 1964):

$$k_G^r = \frac{k_r}{G} = \frac{7.5\pi h}{\ln\left(\frac{r_o}{r_i}\right)}\left[1 + \frac{0.0097h^3}{(r_o - r_i)^3}\right] \tag{4.37}$$

Adkins and Gent proposed the following empirical equation (Davey & Pane, 1964):

$$k_G^r = \frac{k_r}{G} = \frac{H\pi h\left[\left(\frac{r_o}{r_i}\right)^2 + 1\right]}{J\left[\left(\frac{r_o}{r_i}\right)^2 + 1\right]\ln\left(\frac{r_o}{r_i}\right) - M\left[\left(\frac{r_o}{r_i}\right)^2 - 1\right]} \tag{4.38}$$

where $H = 80$, $J = 25$ and $M = 9$ for a short bush.

Table 4.5: Radial geometric stiffness comparison

	Equation	Geometric stiffness (k_r/G) [m]
Gobel	(4.37)	1.6273
Adkins and Gent	(4.38)	0.9717
Finite element method		1.1360

Using the above stiffness values in Table 4.5 it was estimated that the maximum angle would be less than 7°, which seems adequate.

The most advantageous feature of this design is that assembly is much simpler than previous designs. Previous designs required the assembly of two cylinders that moved inside one another, which complicated both assembly and manufacture. The type I design, however, uses spacing rods to separate the two reservoirs, as shown in Figure 4.36. The port is connected via a cradle to the actuator. The cradle assembly was designed to be stiff so that it would not influence the response of the handle. Either end could have been connected to the handle or the actuator, but the most benefit will be gained by connecting the heaviest part to the handle. By connecting it in this way the mass on the drill side is 5.39 kg and on the handle side 7.46 kg. The mass of the hand was ignored during design and testing since it will have a very small effect.

For the type I AVAI it was decided to use water as the absorber fluid. Other possible heavy liquids are listed in the Appendix D. To minimise corrosion, a small amount of glycol was added to the water. The effect of the glycol on the density of the mixture was negligible. The effect of port inlet and outlet geometry is to increase the isolation frequency and was analysed in Du Plooy (1999). For this design the effect of the port geometry is small and can be neglected.

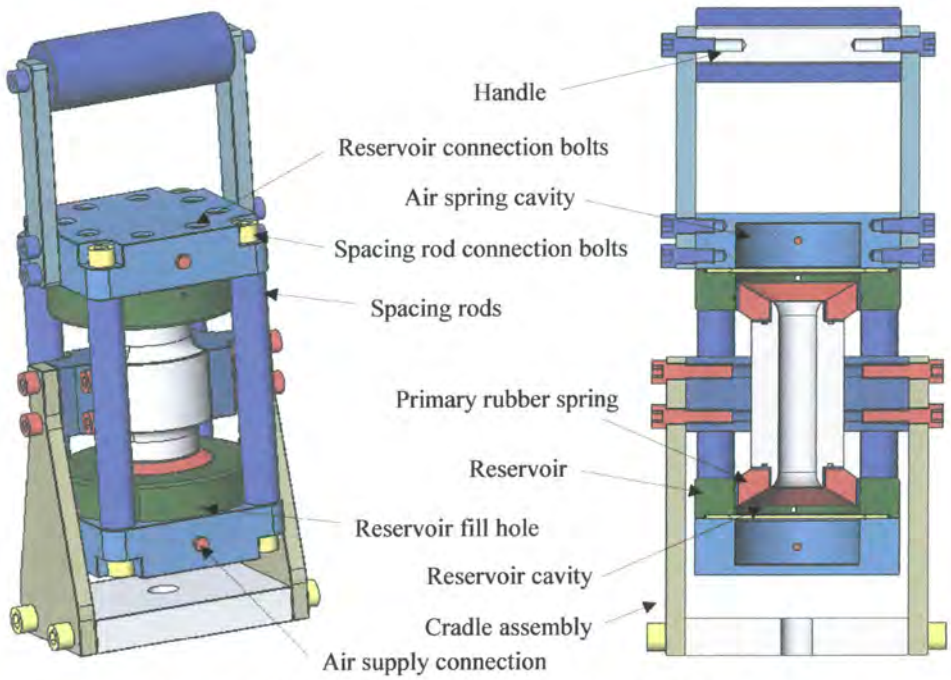

Figure 4.36: Important features of the type I AVAI design

A major problem in previous designs was leakage of the absorber fluid. Leakage occurred because the bond between the metal and the polyurethane spring used in that design failed after a small number of cycles. To ensure that this does not happen the primary spring was press-fitted and sealed using O-rings as shown in Figure 4.37. The press-fit was also required because the natural rubber used in this design could not be bonded to a thick metal part.

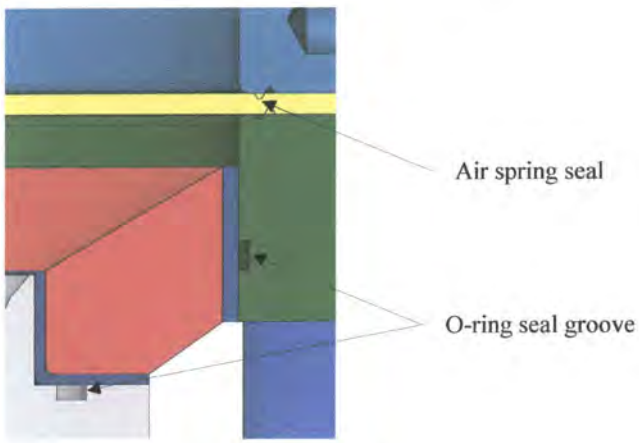

Figure 4.37: Seals for the air spring and reservoir area

An exploded view of the type I AVAI is shown in Figure 4.38.

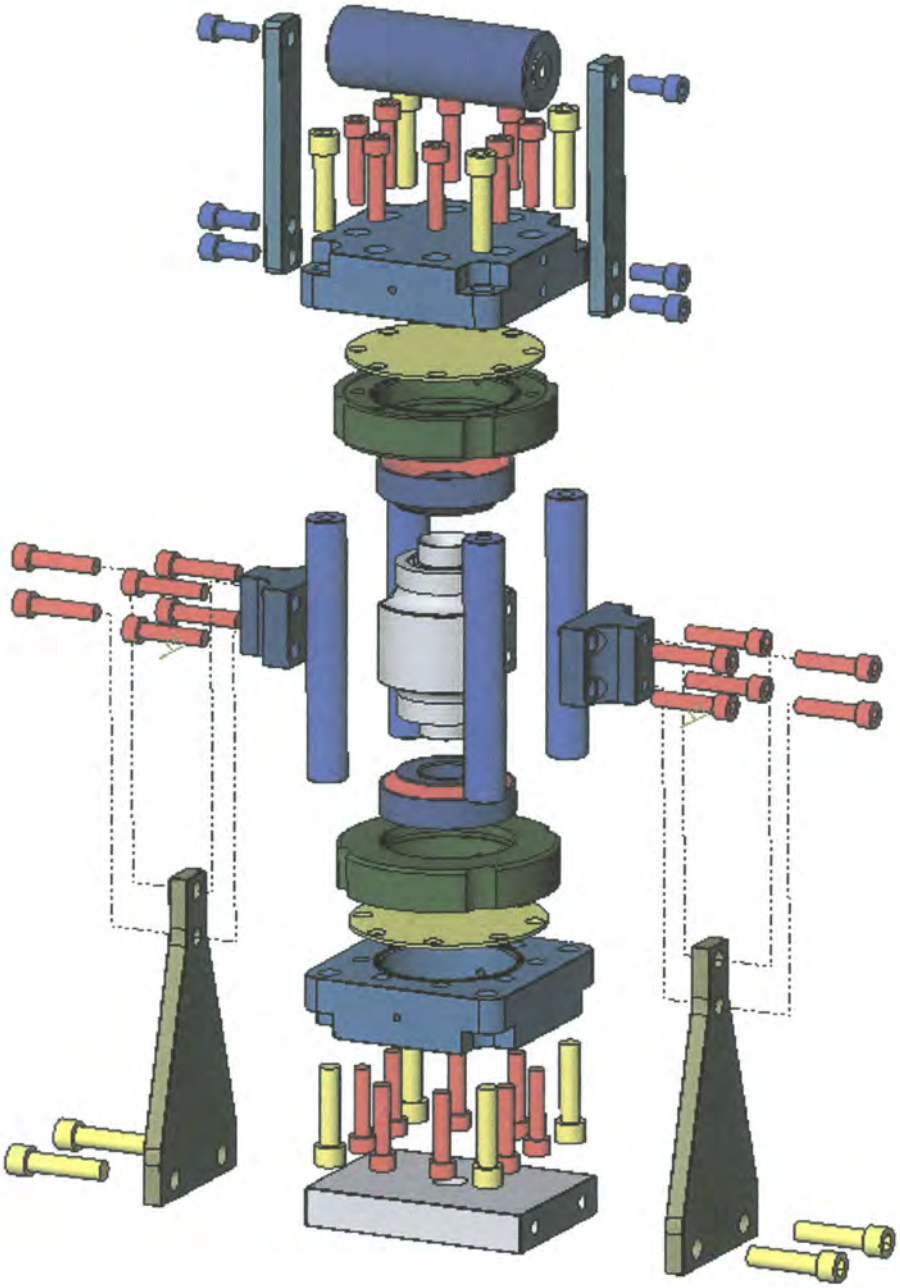

Figure 4.38: Exploded view of the type I AVAI

The major dimensions of the AVAI, are shown in Figure 4.39. The length of the AVAI is determined by the space needed for the operators hand, the port, reservoir and air spring length and the gap needed between the AVAI and the back of the drill. The length of the air spring and reservoir was discussed before. The gap between the drill and the handle is determined by the amplitude of the displacement of the drill, which was estimated to be a maximum of 8 mm. The length of the port is determined by the ratio of port and reservoir diameters. It is possible to shorten the device by increasing the diameter, but this will decrease the distance between the springs, which will affect its rotation angle when the moment is applied.

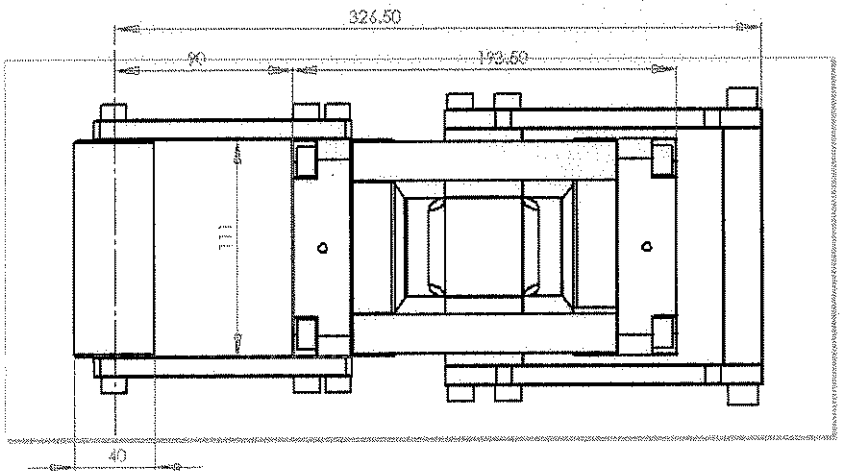

Figure 4.39: Major dimensions

The design dimensions are shown in Figure 4.40. A large air spring height was chosen because it could easily be made smaller later, while making it larger would be difficult. In fact, after testing the spring height was changed to 5 mm by fixing a plastic disc inside the spring.

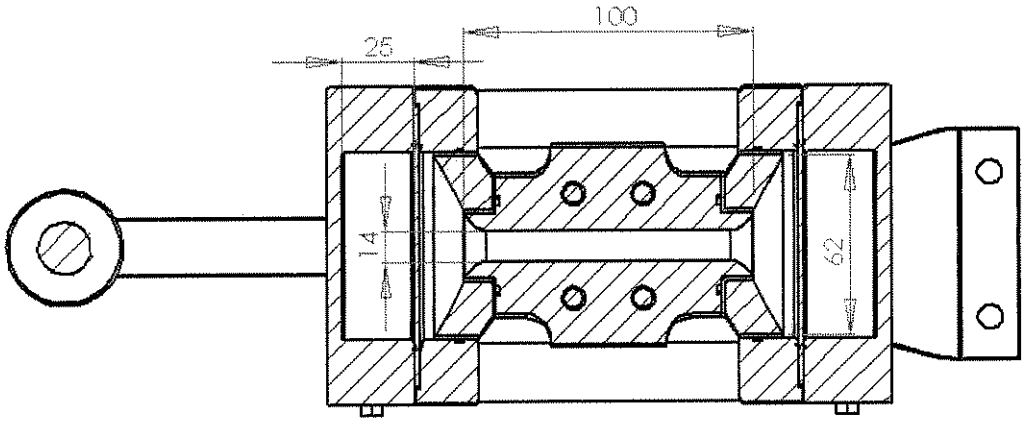

Figure 4.40: Design dimensions

The preceding section showed how the spring stiffness of the primary spring and the air spring could be estimated. Although the formulas could be used for an initial design, it is clear that there is some uncertainty in the exact values. For this reason the absorber will be designed so that it can be modified easily. After manufacture it is possible to reduce the air spring height as well as the port diameter.

The effect of the air spring can be examined by considering the total stiffness of the two rubber membranes and the air spring (Equations (4.19) and (4.20)):

$$k_u = 2\frac{64\pi E t^3}{3d_b^2\left(1-\nu^2\right)} + \frac{2nP\frac{A_b}{3}}{h} \tag{4.39}$$

where t is the membrane thickness, $d_b = 62$ mm is the reservoir diameter, $h = 25$ is the reservoir height, n is the ratio of specific heats and P is the pressure in the air spring and is assumed to be equal to the supply line pressure during steady state operation. For an operating pressure between 300 and 600 kPa the membrane stiffness will be between ~5 and 45 times less than the air spring stiffness. The choice of membrane material should be such that the stiffness of the membrane is minimised while providing an adequate seal under the severe environmental conditions of a mine. The reason for minimising the membrane stiffness is to reduce its contribution to the total damping of the air spring. Lubricants in the air supply rule out the use of natural rubber. Typical elastomer sheet materials are Nitrile and silicone and both can be used in this application. The effect of the air spring height on the isolation frequency can be found by solving the air spring stiffness and then calculating the isolation frequency:

$$\omega_i = \sqrt{\frac{1}{\left(\frac{1}{\bar{\omega}_1}\right)^2 + \frac{1}{\mu_k}\left(\frac{1}{\bar{\omega}_2}\right)^2}} \tag{4.40}$$

When calculating the frequencies in the above equation the area ratio used is the reduced area ratio that compensates for the conical geometry of the primary spring. The reduced area ratio is:

$$A_r = \frac{1}{3}\frac{A_b}{A_a}\left[\left(\frac{d_o}{d_b}\right)^2 + \frac{d_o}{d_b} + 1\right] \tag{4.41}$$

where $d_o = 30$ mm is the inner diameter of the conical section, A_a is the port diameter defined by $d_a = 14$ mm. The effect of air spring height on the isolation frequency is shown in Figure 4.41.

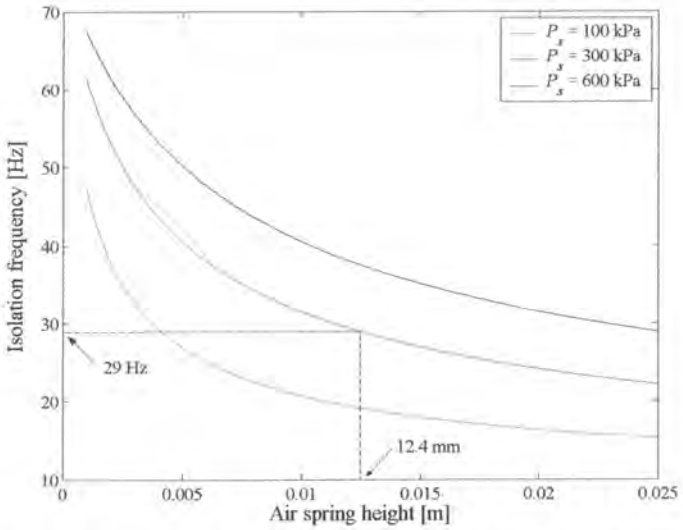

Figure 4.41: Isolation frequency *vs.* air spring height

The frequency range covered by the change in pressure is a function of the air spring height. The required frequency change from 300 to 600 kPa is ~8.5 Hz with the isolation frequency equal to 29 Hz at 300 kPa. Figure 4.42 shows that heights between 2.7 and 13 mm will have the required range.

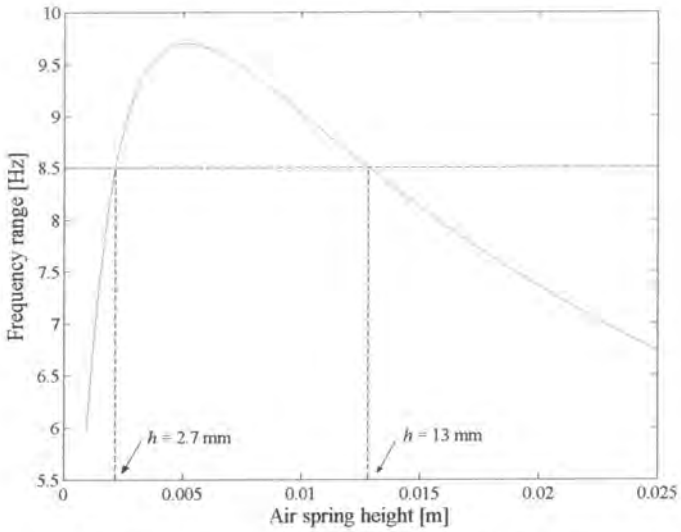

Figure 4.42: Frequency range (P_s = 300 and 600 kPa) *vs.* air spring height

By choosing the air spring height to be 13 mm the isolation frequency will be close to the excitation frequency (refer Figure 4.12) over a wide frequency range, as shown in Figure 4.43. Also shown in the figure is the bandwidth, which can be seen to envelop most of the excitation frequencies. The damped and undamped isolation frequencies are plotted and since the difference is small it is recommended that the undamped isolation frequency be used for design purposes. In production there will be significant differences between individual AVAIs. To compensate for this the AVAI could be designed with an air spring height that can be varied externally with a mechanism. Each AVAI can then be tuned before being used. Tuning could also be effected by keeping the air spring at atmospheric pressure and varying its height, as shown by Ting-Kong (1999).

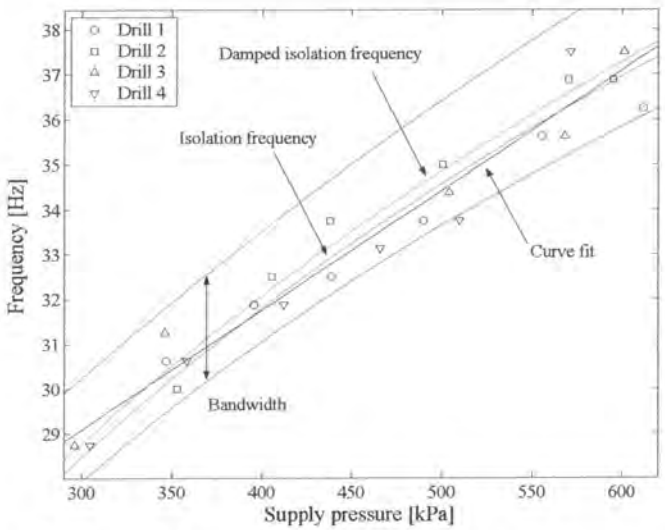

Figure 4.43: Excitation and isolation frequency *vs.* supply line pressure (h = 13 mm)

To estimate the benefit of adding an AVAI, the response to the measured excitation was simulated. Three cases were considered. In the first case the device is tuned using the supply line pressure i.e. the spring stiffness as a function of air spring pressure shown in Equation (4.39) was used. This should be the least effective method since differences between individual drills and the estimated average is not taken into account as can be seen from Figure 4.43. A second simulation shows the effect when the AVAI is tuned using a control system that forces coincidence of the isolation and excitation frequencies while the damping ratio is kept constant. The excitation frequency is determined by calculating the FFT of the input excitation and finding the frequency at which the maximum occurs. The transmissibility is then minimised at the excitation frequency using an optimisation algorithm to calculate the optimal stiffness. The third case employs a control system to minimise the weighted rms acceleration by adjusting both the stiffness and the damping. The simulation used the PSD method to calculate the weighted rms acceleration. The weighted rms was minimised using both the stiffness and damping as variables in an optimisation algorithm. The methods are summarised in Table 4.6.

Table 4.6: Summary of tuning methods

Method	Stiffness	Damping
1	Derived from supply line pressure	Constant
2	Optimal	Constant
3	Optimal	Optimal

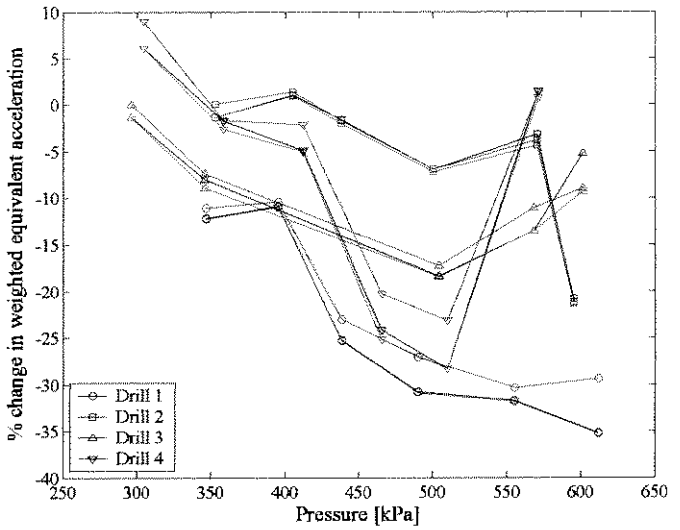

Figure 4.44: Percentage change in the weighted equivalent acceleration with the addition of a type I AVAI using the supply line for tuning (red), tuning the device using the excitation frequency (black) and perfect tuning (blue)

The percentage change in weighted rms acceleration for an AVAI tuned using the supply line pressure only is shown in Figure 4.44 in red. The most benefit is achieved at higher pressures and at best a ~35% reduction was achieved. At low pressures it is possible that the AVAI can increase the weighted equivalent acceleration. The percentage change in weighted equivalent acceleration for an AVAI tuned to the excitation frequency is shown in Figure 4.44 in black. This result is better than if the supply line

only was used. This case does not necessarily represent the maximum benefit possible, since a situation can exist where a detuned AVAI results in lower weighted rms acceleration.

For such a case the objective function will be the weighted rms acceleration and most ideally, both the stiffness and damping will be adjusted to minimise this quantity. A typical objective function for such a case is shown in Figure 4.45. Clearly, a minimum value does exist and if the AVAI can be adjusted to this value it will be perfectly tuned for this application. Simulation for a perfectly tuned case found that there is little benefit in choosing such a method. This is shown in Figure 4.44 in blue. This might not always be the case and for some applications it could be beneficial to use such an objective function instead of more simplistic methods. The net result of tuning the type I AVAI using the supply line pressure is shown in Figure 4.46. The target of 10 m/s^2 is not reached in the majority of circumstances.

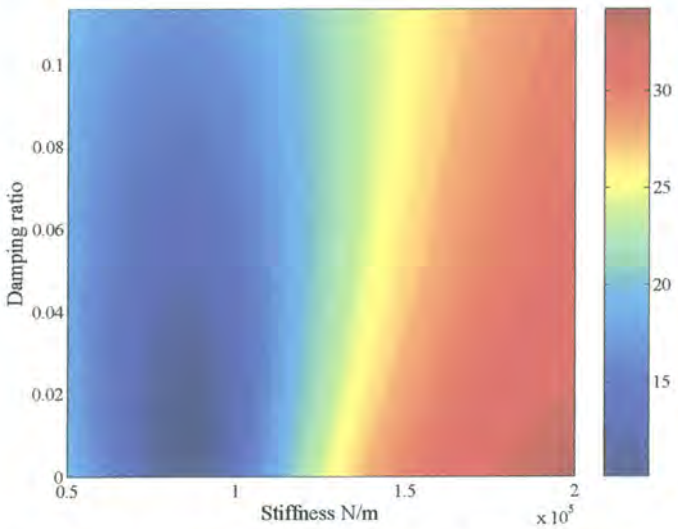

Figure 4.45: A typical objective function for an AVAI with adjustable stiffness and damping

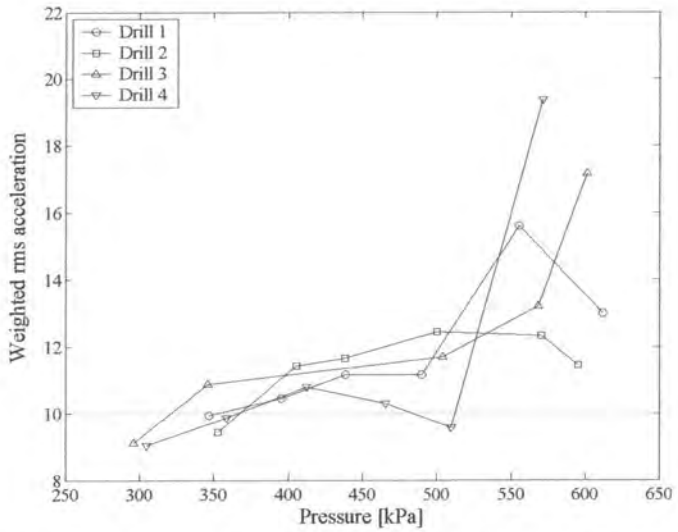

Figure 4.46: Simulated weighted rms acceleration for a type I AVAI tuned using the supply line pressure

4.5 Type II amplified vibration-absorbing isolator

This section will document the design of the type II absorber, where initially the effect of noise in the input will be assessed and thereafter the actual design will be discussed.

4.5.1 Narrow-band excitation with noise

The parameters used in the comparison between the type II AVAI and an isolator is shown in Table 4.7. The isolator stiffness ratio was held constant at the lowest value used for the tuned AVAI to allow for fair comparison. For each case the AVAI was tuned to the centre of the excitation frequency ($\bar{\omega}_e$) by changing the stiffness ratio. A comparison of the isolator and type II AVAI are shown in Figure 4.47.

Table 4.7: Parameter values used for the comparison

Description	Parameter	Value
Centre frequency of excitation	$\bar{\omega}_e$	10
Frequency bandwidth	$\Delta\Omega_e$	20
Mass ratio	ω_n/ω_i'	0.5
Stiffness ratio	μ_k	21.6...25

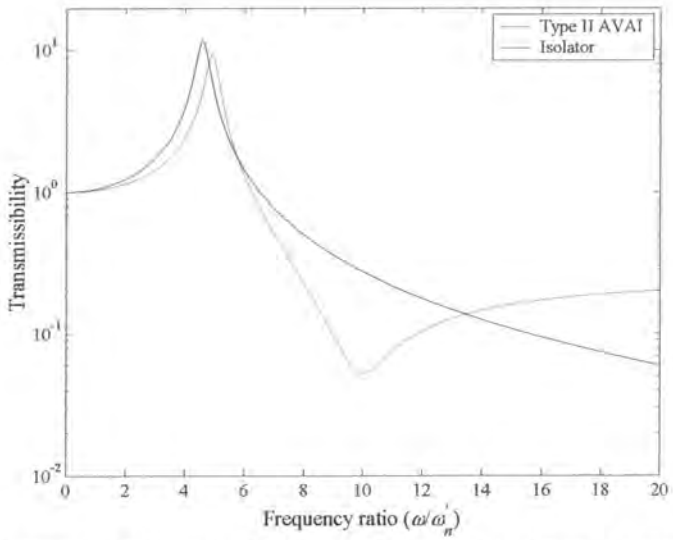

Figure 4.47: Type II AVAI and isolator used in the comparison

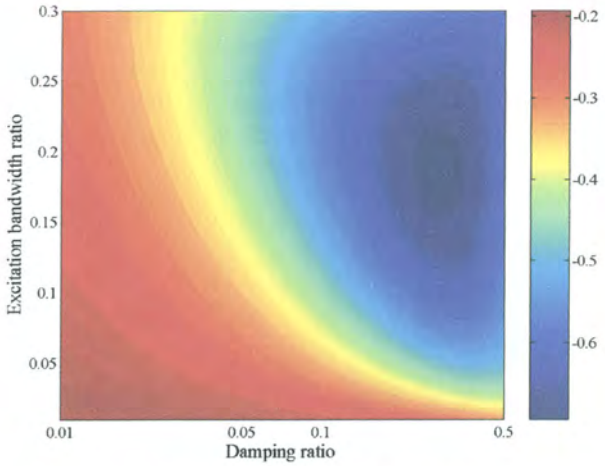

Figure 4.48: The logarithm of the ratio of ratios for a case with noise ratio 10^{-3}

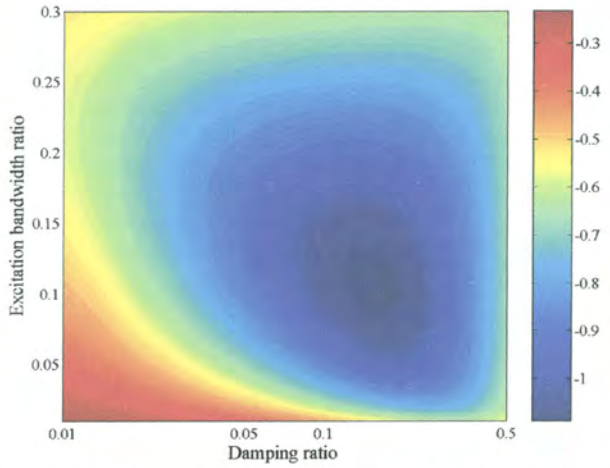

Figure 4.49: The logarithm of the ratio of ratios for a case with noise ratio 10^{-4}

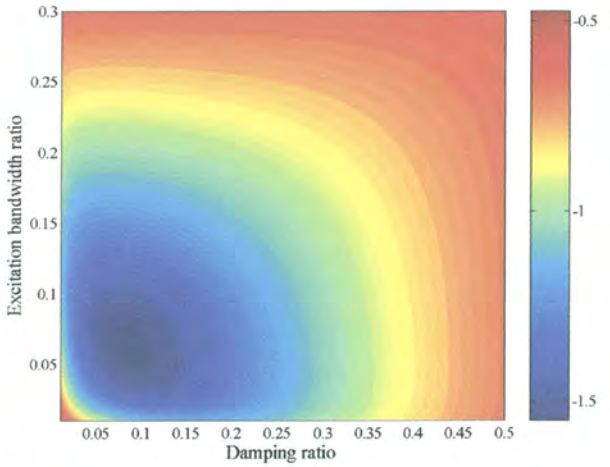

Figure 4.50: The logarithm of the ratio of ratios for a case with noise ratio 10^{-5}

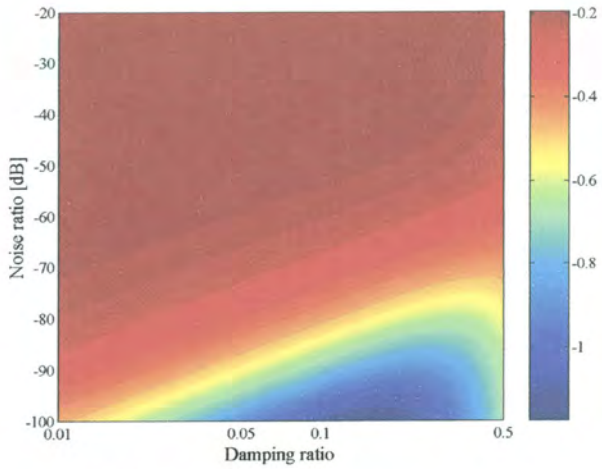

Figure 4.51: The logarithm of the ratio of ratios for a case with excitation bandwidth ratio 0.01

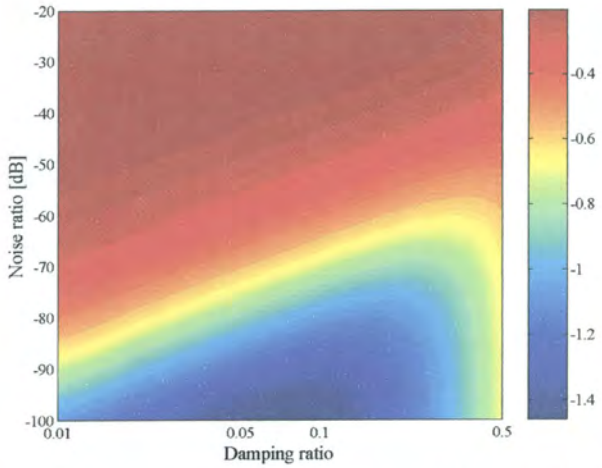

Figure 4.52: The logarithm of the ratio of ratios for a case with excitation bandwidth ratio 0.1

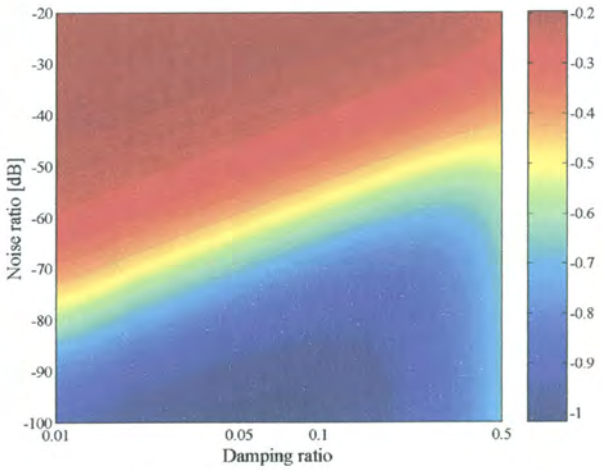

Figure 4.53: The logarithm of the ratio of ratios for a case with excitation bandwidth ratio 0.2

Figure 4.48 through Figure 4.50 show the damping required as a function of excitation bandwidth ratio when the noise ratio is kept constant. The figures show that as the noise ratio is increased, more damping is needed. It also shows that the benefit of using an AVAI is the most at small noise ratios and small excitation bandwidth ratios. Figure 4.51 through Figure 4.53 confirm that the damping must be increased as the noise ratio increases. Figure 4.48 through Figure 4.53 show that an optimal value of damping exists for each noise and excitation bandwidth ratio. In each of the cases considered here it was more advantageous to use a tuneable AVAI. As was discussed in §4.4.1, it will be difficult to prescribe a damping ratio during the design process.

4.5.2 Type II AVAI design

A schematic of the type II AVAI is shown in Figure 4.54. It consists of a port with a Teflon bearing in which a tungsten carbide slug with a sliding fit is mounted. The tungsten carbide is ground to a smooth finish and has a density of ~14500 kg/m^3. The Teflon bearing is press-fitted and then machined to provide the sliding fit. The air spring is similar to the one used in the type I AVAI and consists of a pressure supply line connected to the air spring cavity via an orifice. The reservoir is filled with fluid, which transfers the motion to the slug, resulting in the amplification of the slug motion. Preferably the fluid will have low viscosity and provide some lubrication, but due to the filling method used it was not possible to use oil, and water had to suffice. A small gap exists between the slug and the Teflon bearing through which leakage can occur. The initial design proposed the use of slug stops as shown in Figure 4.55. The purpose of the slug stop is to equalise the volume of fluid in the two reservoirs. After considerable difficulty with the experimental work it was decided to replace these with slug springs. The only disadvantage of using slug springs is that they can add damping to the system through turbulence in the fluid. They will also cause an increase in the isolation frequency, but by choosing their stiffness to be small this effect will be negligible.

It may be possible to provide a positive seal between the slug and the port by using a metal bellow or a rolling diaphragm seal, but this will be costly. The large amplitude and number of cycles needed might even make this method infeasible. It could also be possible to provide a pressure-activated leakage path between the two reservoirs. When the slug impacts the stop, leakage will occur between the two reservoirs. Instead of becoming completely solid, the leakage will provide additional damping and decrease the shock load due to the impact.

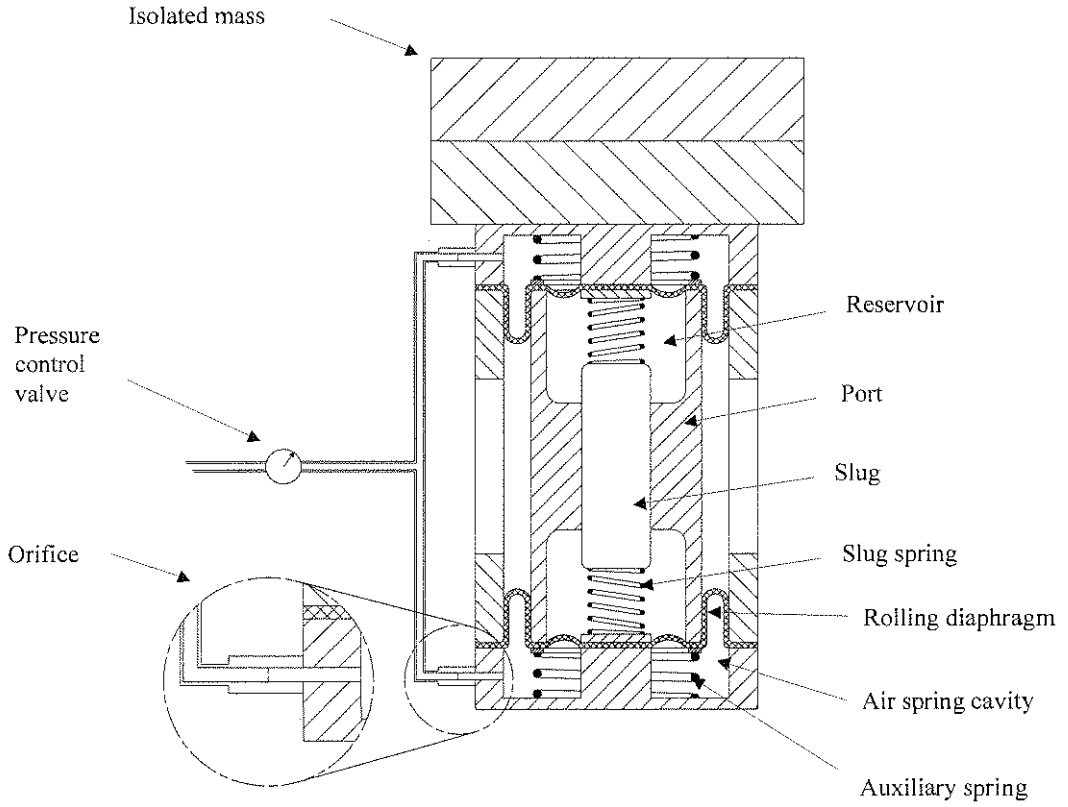

Figure 4.54: Schematic of type II AVAI design

The flexibility between the port and the reservoir is provided by a rolling diaphragm seal. This seal also acts as the air spring boundary. Rolling diaphragms are zero-leakage seals that offer very little frictional damping since the relative motion between the seal and the contact surface is small. Additionally, the diaphragms are reinforced with polyester that do not stretch and will therefore have a low loss factor. These seals have a limited number of standard sizes, which will put a constraint on this design that was not present for the type I AVAI.

The volume of the spring is determined by the average of the inner and outer diameter of the rolling diaphragm and the diameter of the inner diaphragm mount as shown in Figure 4.55. The port and the groove in the sleeve must be machined according to the manufacturer's specification to ensure that the diaphragms seal properly and have adequate durability. When the seal rings are fitted the seal tends to bulge. This is advantageous because it provides some low stiffness flexibility between the reservoir and the port. The maximum relative amplitude is ~2 mm. The maximum motion possible can be increased by fitting a custom made diaphragm with a second convolution in the reservoir area. This second convolution should face towards the air spring as shown in Figure 4.56. Such a diaphragm configuration will however make it impossible to transfer a moment from the handle to the drill. As discussed in §4.2 the drill handle must transfer a large moment and this will have to be done in some different way if this method is used.

It is possible to provide a bearing to transfer the moment. The bearing will have to be low friction such as a linear ball bearing or an air bearing. An air bearing could work well since air is readily available, but air consumption must be low for it to economically feasible. However, the space available for an air bearing is also very limited.

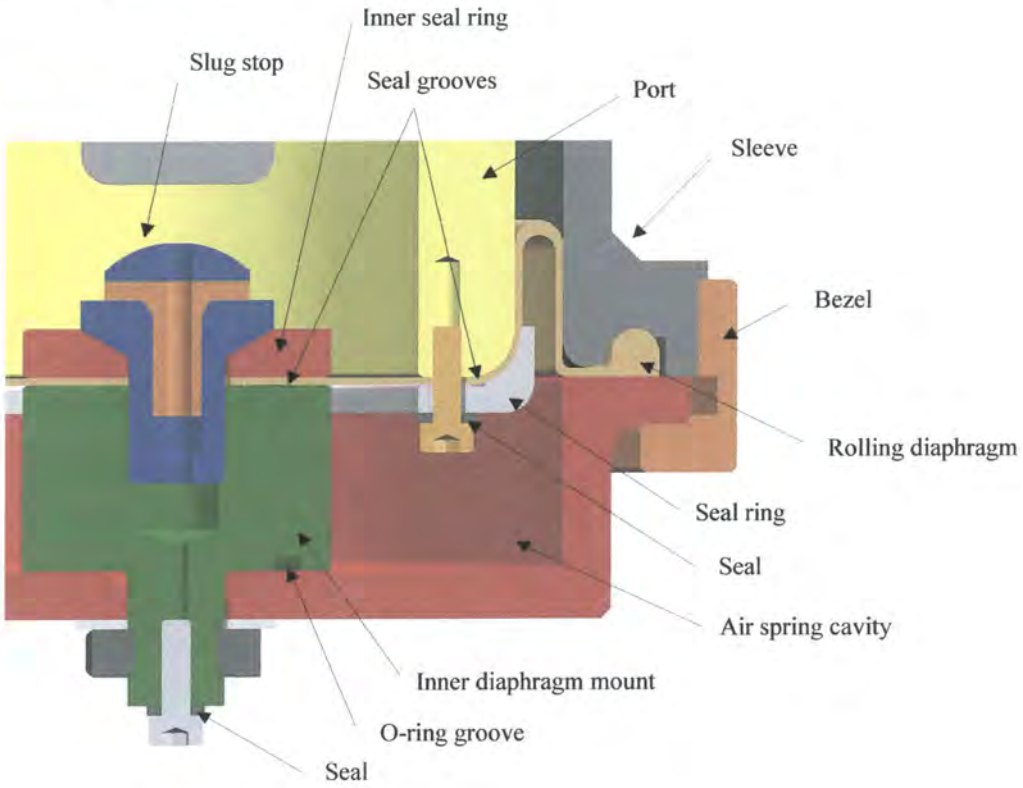

Figure 4.55: Air spring design

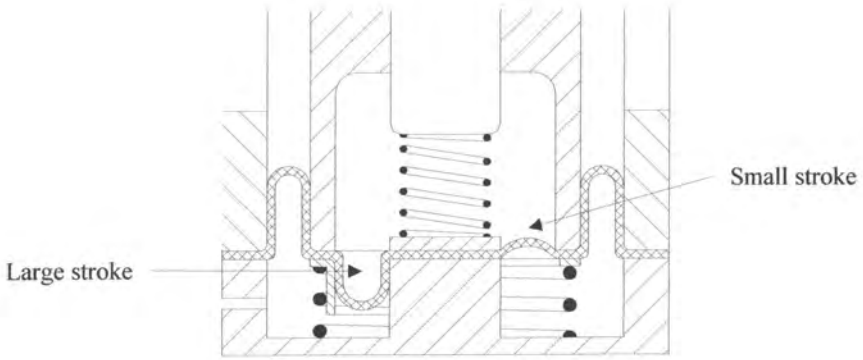

Figure 4.56: Possible diaphragm designs

The purpose of the auxiliary spring in Figure 4.54 is to centre the port vertically. In an application where the load is not variable the auxiliary spring will be chosen to off-set the mass of the supported machine. Under variable load the springs must ensure that the port will always be in a position where the maximum displacement amplitude can be accommodated.

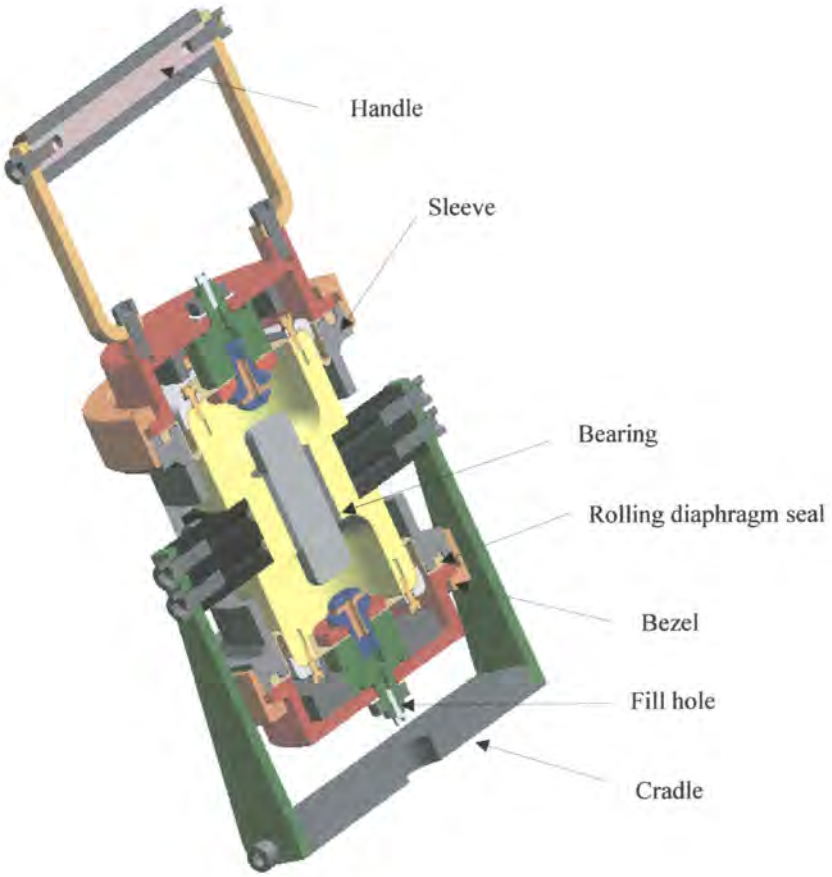

Figure 4.57: Important features of the type II AVAI design

The reservoir must be filled without trapping air bubbles, which will be compressible and decrease the effective reservoir area. This proved to be a challenge. Options available include pressurising the fluid in the reservoir, vacating the air in the reservoir cavity before filling it with fluid, or assembling the reservoir parts while submerged. The last method is difficult to execute, but does not put additional strain on the design and was therefore preferred. Securing the air spring cavity to the sleeve can be done in a number of ways, as long as the rolling diaphragm seal can be accommodated. For this design it was decided to use a bezel rather than bolts on a flange to reduce the diameter of the device as shown in Figure 4.55. Because the bezel was chosen the air spring cavities were not separated by spacing rods as for the type I design, but by a flanged section of hollow bar (sleeve) as shown in Figure 4.57. The sleeve was also necessary to provide a supporting surface for the rolling diaphragm.

Freudenberg's standard rolling diaphragms are available from an outer diameter of 16 mm up to 200 mm. To ensure optimal use of space the reservoir diameter must be as large as possible, but it is limited by the sealing requirements for the diaphragm seal. The seal is bolted onto the port using a seal ring. Four M3 cap screws were used which proved difficult to work with (smaller crews should not be considered). To ensure that no leakage occurs at the cap screw a washer was added which consisted of

a flat metal ring with an internally bonded trapezoidal rubber seal. Initially the holes were positioned too close to the reservoir and it did not seal properly. The holes were moved closer to the radius, which solved the leakage problem. Thus, with significant difficulty the diameter of the reservoir could be maximised to 50 mm using a 70 mm inside diameter rolling diaphragm. The rolling diaphragm is relatively fragile and caution must be exercised not to twist it while tightening the bezel or the inner seal ring.

If it is assumed that the diaphragm deforms as shown in Figure 4.58, an effective reservoir area can be calculated.

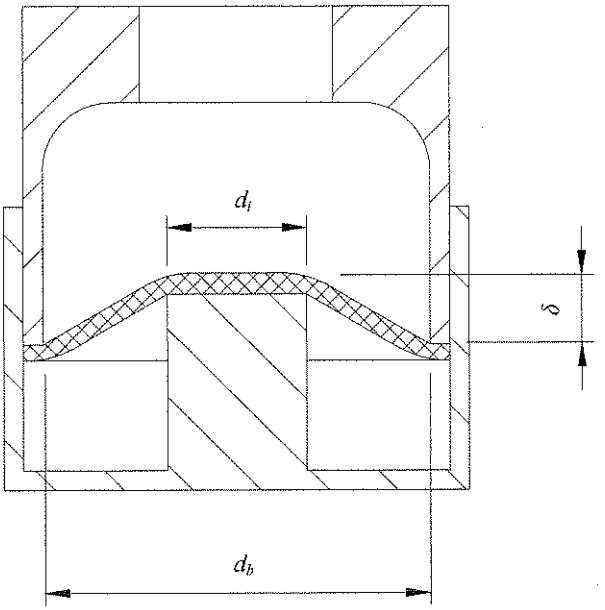

Figure 4.58: Dimensions for the calculation of the effective area

The effective reservoir area is [Equation (D.14)]:

$$A_e = \frac{\pi}{12}\left(\frac{d_b^3}{d_b - d_i} - \frac{d_b d_i^2}{d_b - d_i} + d_i^2\right) \tag{4.42}$$

The effective area ratio can be maximised by choosing the inner diameter d_i as large as possible. A large inner diameter will, however, limit the displacement that can be achieved. The major dimensions of the design are shown in Figure 4.59 and Table 4.8. The device is smaller and considerably lighter than the type I design. Two slugs were manufactured; one with a diameter of 16 mm and one of 20 mm. Changing the slug size requires the remanufacture of the bearing only.

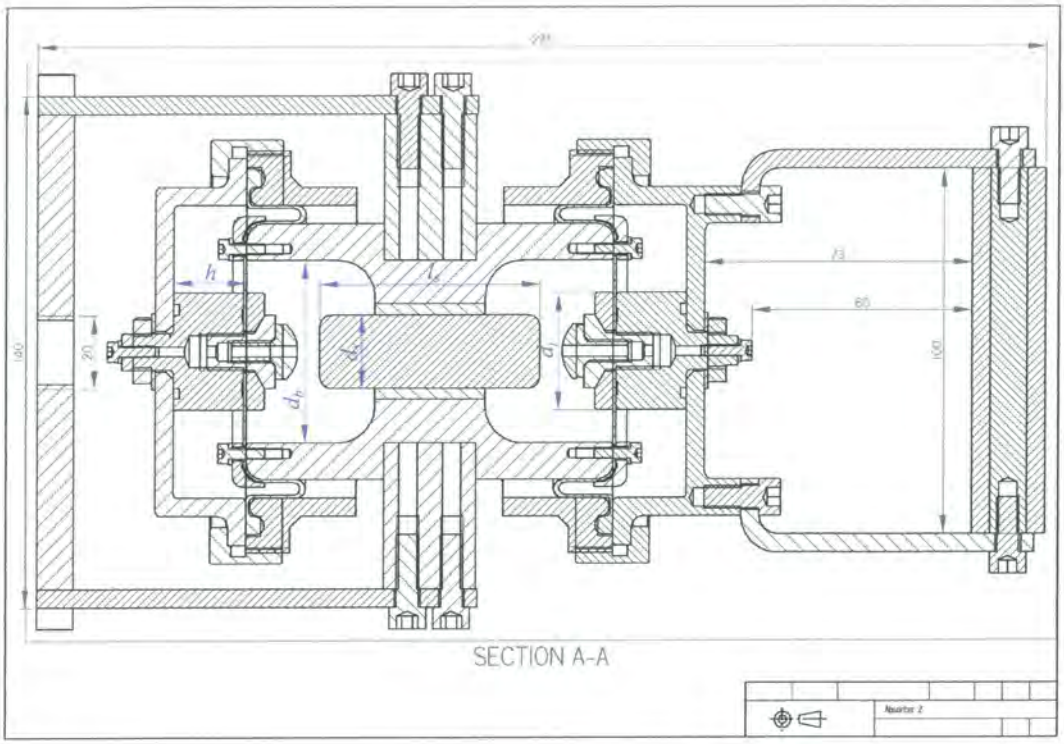

Figure 4.59: Major dimensions of the type II AVAI

Table 4.8: Type II design parameters

	Variable	Value
Slug diameter [mm]	d_s	16, 20
Reservoir outer diameter [mm]	d_b	50
Reservoir inner diameter [mm]	d_i	32
Isolated mass [kg]	m	3.5
Density [kg/m^3]	ρ	14500
Slug length [mm]	l_s	60
Effective area ratio	A_e/A_a	4.27, 6.67
Air spring outer diameter [mm]	d_s	75
Air spring height [mm]	h	20
Damping ratio	ζ	0.05

The travel required by the slug is dependent on the area ratio and the input displacement as shown in chapter 2. The AVAI is designed for a base input of 2 mm as discussed in §4.3. Assuming that the device is perfectly tuned and including the effects of damping, the relative displacement between the handle and the base is 1.74 mm. The slug travel will be 7.43 mm for the 20 mm slug and 11.61 mm for the 16 mm slug. The present design has provision for 12 mm of travel, which is deemed adequate for prototype purposes.

The design requires that the damped isolation frequency coincide with the excitation frequency for all the supply pressures. If no auxiliary spring is used then the results will typically be as shown in Figure 4.60. It is not possible to change the slope and the y-axis intercept independently by only changing the

air spring dimensions. One possibility is to change the area ratio or slug diameter in conjunction with the air spring dimensions. Since there are several implications when changing these values, for instance, slug travel, it is proposed that an auxiliary spring should be used instead. The air spring height and the auxiliary spring stiffness can now be used to independently change the slope and y-axis intercept. The total stiffness can be written as:

$$k = k_p P_s + k_c \tag{4.43}$$

where k_p is the coefficient defining the air spring dimensions and k_c represents the auxiliary spring. The values for k_p and k_c can be calculated by considering two sets of supply pressure (P_s) and excitation frequency (Ω_e) data points defined by the curve fit in Figure 4.60 [Equation (D.21)]:

$$\begin{bmatrix} k_p \\ k_c \end{bmatrix} = \frac{\left[m + m_B \left(\frac{A_b}{A_a} \right)^2 \right]}{\frac{-\left(\frac{\omega_n}{\omega_i} \right)^2 - 1 - \sqrt{\left[\left(\frac{\omega_n}{\omega_i} \right)^2 - 1 \right]^2 + 8\zeta^2 \left[\left(\frac{\omega_n}{\omega_i} \right)^2 + 1 \right]}}{4\zeta^2 + 4\zeta^2 \left(\frac{\omega_n}{\omega_i} \right)^2 - 2\left(\frac{\omega_n}{\omega_i} \right)^2}} \begin{bmatrix} P_1 & 1 \\ P_2 & 1 \end{bmatrix}^{-1} \begin{bmatrix} \Omega_{e1}^2 \\ \Omega_{e2}^2 \end{bmatrix} \tag{4.44}$$

The result of such a design is shown in Figure 4.61. The damped isolation curve coincides with excitation frequency curve fit at the design points of 290 and 620 kPa. Instead of using only two points it is also possible to calculate the stiffness to minimise the least squares difference between the isolation and excitation curves. In this case it does not appear to be worth the effort since all the measured excitation frequencies fit comfortably within the bandwidth. Of course, as the damping is reduced the bandwidth will decrease making the matching process more difficult.

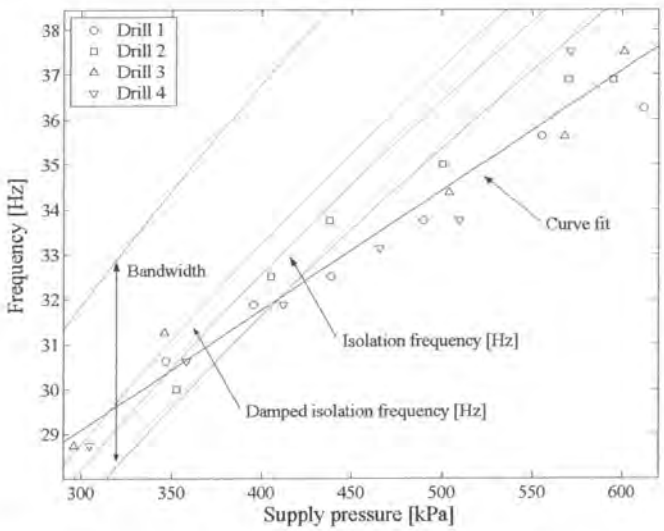

Figure 4.60: Excitation vs. isolation frequency for a system without an auxiliary spring (d_a = 16 mm and h = 14.6 mm)

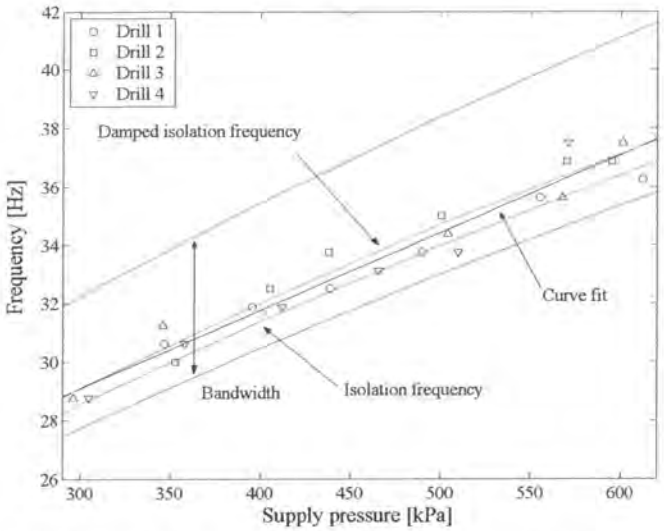

Figure 4.61: Excitation vs. isolation frequency for a system with an auxiliary spring (d_a = 16 mm, h = 22.6 mm and k_c = 80320)

When the design is complete the challenge that remains is to manufacture an airspring and auxiliary spring that fit the specifications. Tolerance values on springs, helical or otherwise, can be quite large and it would be necessary to tune each device at considerable expense. Of course, if a control system is used, exact matching becomes less important since the control system can compensate. In such a case the initial design only needs to be in the vicinity of the frequency range covered as long as it is exceeded by the device's isolation frequency range capability.

The performance of a system tuned using the supply line is shown in Figure 4.62 in red. The benefit ranged from 5% to 50%, but importantly it was never detrimental as in the case of the type I AVAI. By tuning the device to the excitation frequency only slight benefit is gained as shown in Figure 4.62 in black. When optimising both the damping and stiffness to minimise the weighted rms acceleration the performance is significantly better, as indicated by the blue curve. This is in contrast with the type I AVAI where the gain was not considerable. The weighted rms acceleration with the addition of the type II AVAI is shown in Figure 4.63. The acceleration values are below 10 m/s^2 at low supply pressure.

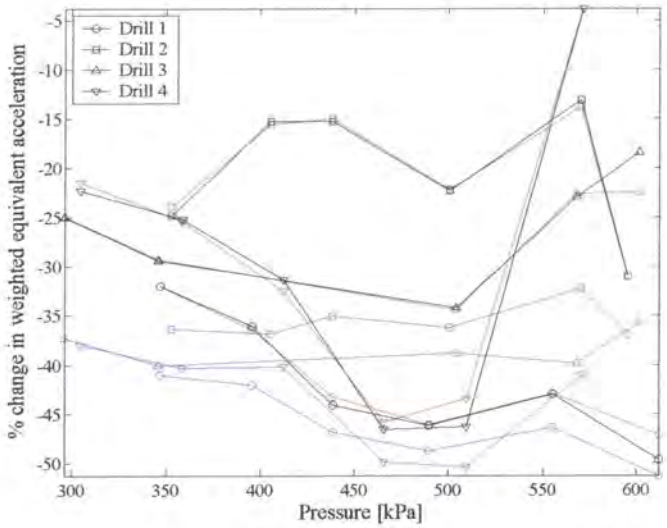

Figure 4.62: Percentage change in the weighted equivalent acceleration with the addition of a type II AVAI using the supply line for tuning (red), tuning the device using the excitation frequency (black) and perfect tuning (blue)

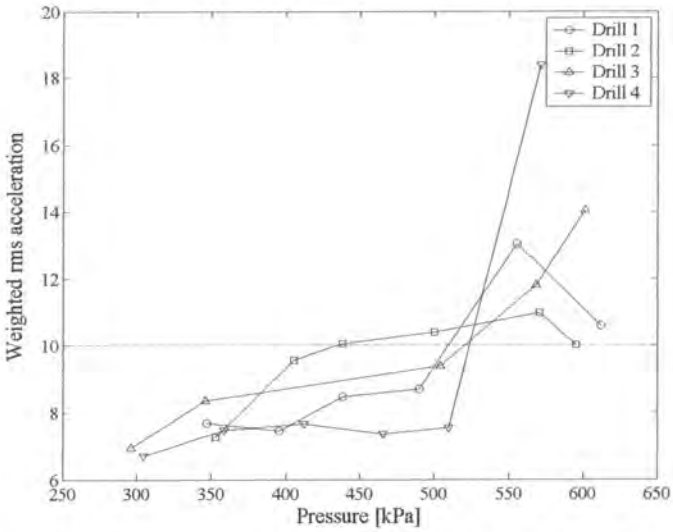

Figure 4.63: Simulated weighted rms acceleration for a type II AVAI tuned using the supply line pressure (PSD method)

4.6 Conclusion

This chapter introduced the concepts applicable to the design of a vibration-isolated handle. The vibration levels of pneumatic rock drills used in the South-African mining industry were shown to be in excess of the exposure limit for short duration rms weighted acceleration permitted under the proposed European Union legislation. Maximum measured values on these drills were 18.72 m/s^2. Two types of vibration absorber were designed and evaluated. Simulation showed that by using a type I AVAI the acceleration levels could be reduced significantly but not to the required levels for all the

drills. The type II AVAI levels were reduced to below 10 m/s^2 up to a pressure of 500 kPa for three of the drills tested. Supply line pressure at the rock face is in South African mines are mostly below 400 kPa.

5 Experimental results

5.1 Introduction

This chapter documents the experimental results of the two AVAIs. The experiments measured the transmissibility in the frequency domain. The results were processed to obtain the parameters that were uncertain during the design process by fitting the analytical models to the experimental results. This will aid future designs of similar absorbers since more accurate models will be available. The experimental set-up measured transmissibility as shown in Figure 5.1. The AVAI was fitted to a hydraulic actuator. Both Zonic and Schenck actuators were used, which were controlled by a custom built PID controller. It was not possible to recreate the amplitudes that the AVAI would experience on a drill, but it was sufficient for characterisation. The air spring was fitted to a 6 bar air supply via a Festo pressure control valve. Accurate pressure readings of the supply pressure were obtained from a strain gauge type GEM pressure transducer. An assortment of PCB ICP accelerometers and signal conditioners were used. A Spectral Dynamics Siglab 20-42 FFT analyser sampled the data. It was also used to supply the various excitation signals.

In the second part of this chapter the manual pressure regulator was replaced by a servo operated valve system that could be controlled with a National Instruments 6024E DAQ card. This was done to show that the device could be used in a closed-loop sense in a system where the excitation frequency can vary arbitrarily.

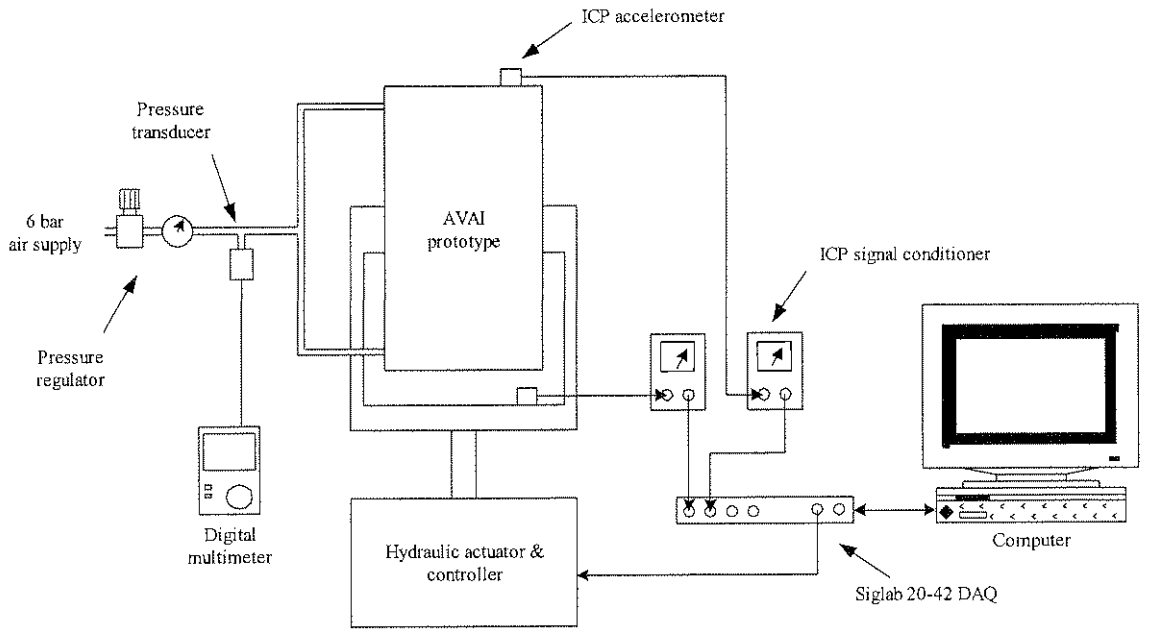

Figure 5.1: Transmissibility measurement set-up

5.2 Type I AVAI

5.2.1 Experimental results

The experimental set-up is shown in Figure 5.2. Here the AVAI was fitted to a Zonic hydraulic actuator and controller. Four 10 kg weights were incrementally added to the AVAI (recall that the mass of the AVAI on the isolated side is 7.5 kg). The stepped sine excitation method was used with a 0.2 Hz frequency resolution from 10 to 70 Hz. This method gave good results, with the lowest correlation measured being 0.98. Acceleration measurements were done with 100 mV/g PCB ICP accelerometers. The pressure was varied using a manual pressure regulator in increments of ~50 kPa from 0 to 600 kPa.

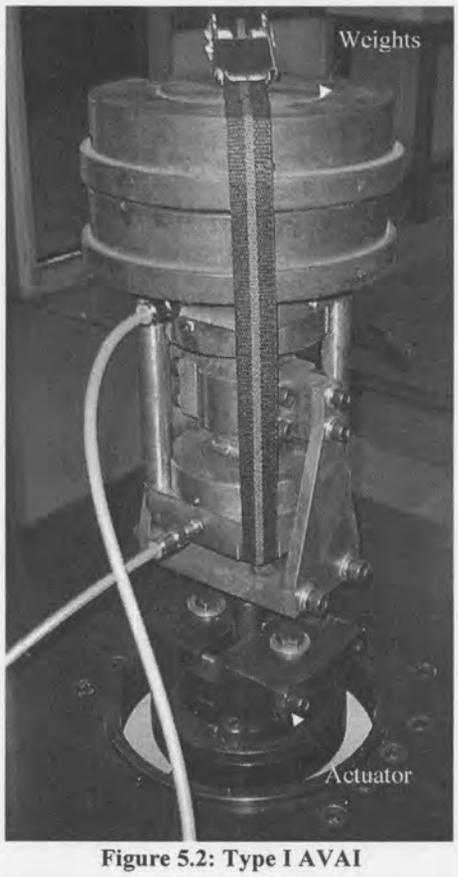

Figure 5.2: Type I AVAI

A set of transmissibility curves measured in this way is shown in Figure 5.3, where it is compared to an undamped conventional isolator with a similar natural frequency as reference. Also shown is a straight-line curve fit through the points off minimum transmissibility at each frequency. These points do not necessarily coincide with the isolation frequency since the minimum transmissibility is also a function of pressure. The points were calculated by finding the intercept of the slope of each curve with the following curve. The envelopes of all the curves are shown in Figure 5.4. As could be expected, the transmissibility is lower as the isolated mass is increased.

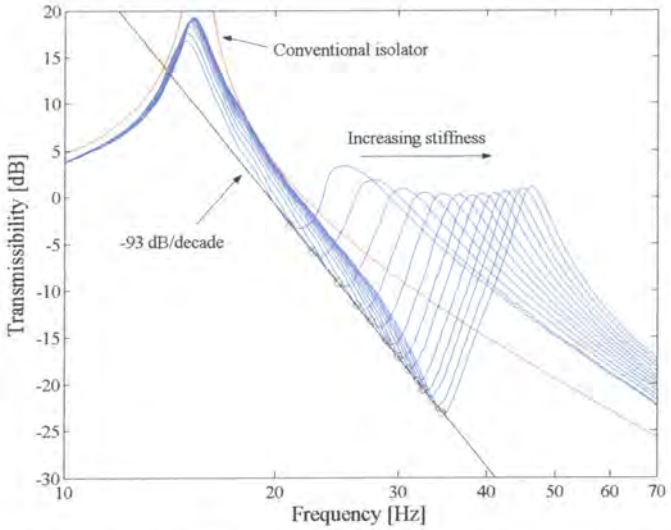

Figure 5.3: Change in transmissibility as the air spring stiffness is increased for a 37.5 kg isolated mass (The red circle indicates the lowest transmissibility at a specific frequency, p_s = ~0..600 kPa)

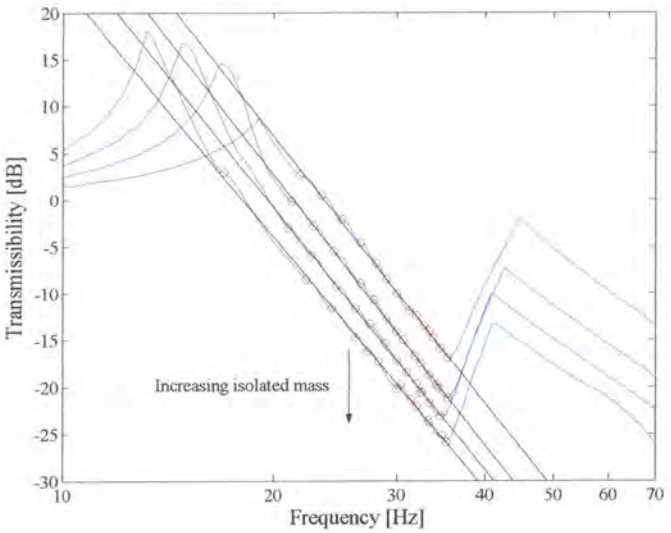

Figure 5.4: Transmissibility curve envelopes for the 4 isolated masses (The red circle indicates the lowest transmissibility at a specific frequency)

When compared to an undamped conventional isolator over the frequency range of the AVAI the performance is significantly better. The calculated roll-off is summarised in Table 5.1.

Table 5.1: Roll-off results

Isolated mass [kg]	Roll-off [dB/decade]
17.5	-94.7
27.5	-95.9
37.5	-93.0
47.5	-89.3

To calculate the isolation frequency and bandwidth from the measured data it was necessary to fit a curve through the data to find an accurate estimate. A typical result of one such 2nd degree polynomial curve fit is shown in Figure 5.5. A number of data points close to the isolation frequency were used for the curve fit. The resulting polynomial was used to find the isolation frequency as well as the frequencies defining the bandwidth (ω_1 and ω_2).

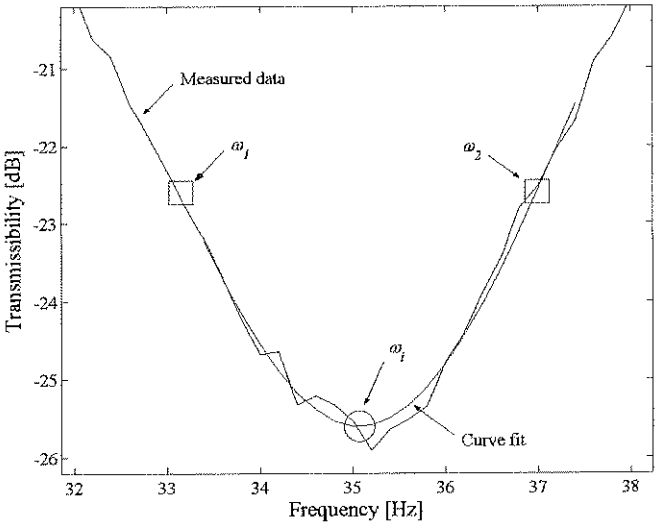

Figure 5.5: Curve fit to calculate the isolation frequency and bandwidth

The isolation frequencies as a function of pressure calculated using this method is shown in Figure 5.6. The AVAI covered a frequency range of ~12 Hz. By fitting a 2nd degree polynomial through the data the following relationship between the supply pressure (p_s in bar) and excitation frequency (f_e in Hz) was found:

$$p_s = 0.0247 f_e^2 - 0.9884 f_e + 9.8658 \tag{5.1}$$

This equation can be used in an open-loop control system.

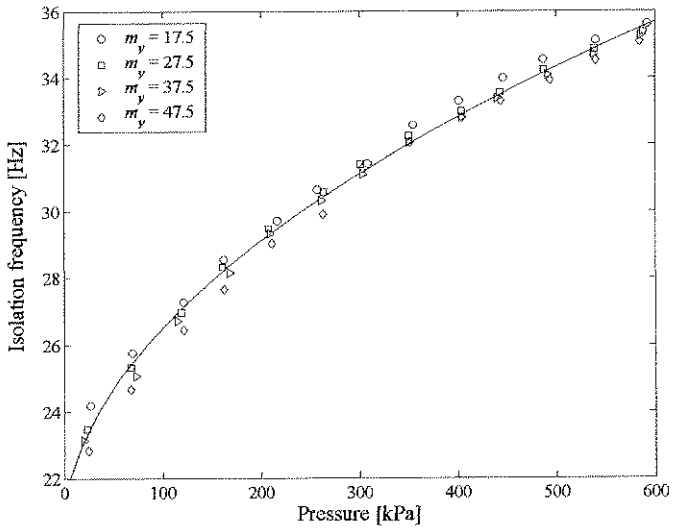

Figure 5.6: Isolation frequency curve fit

The robustness and bandwidth are calculated using the definitions in Equation (2.20) and Equation (2.21) and are shown in Figure 5.7.

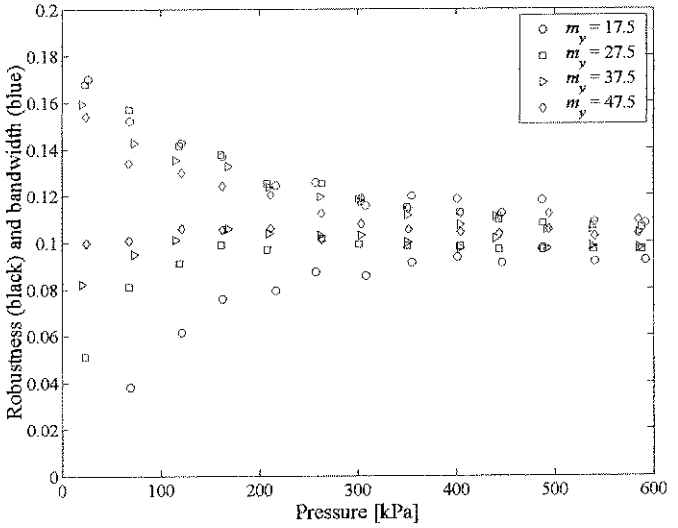

Figure 5.7: Robustness and bandwidth *vs.* supply pressure

The frequency range of the absorber is compared to the drill excitation frequency in Figure 5.8. With some modification it should be possible to ensure that the isolation frequency falls within the 95% confidence intervals of the excitation frequency.

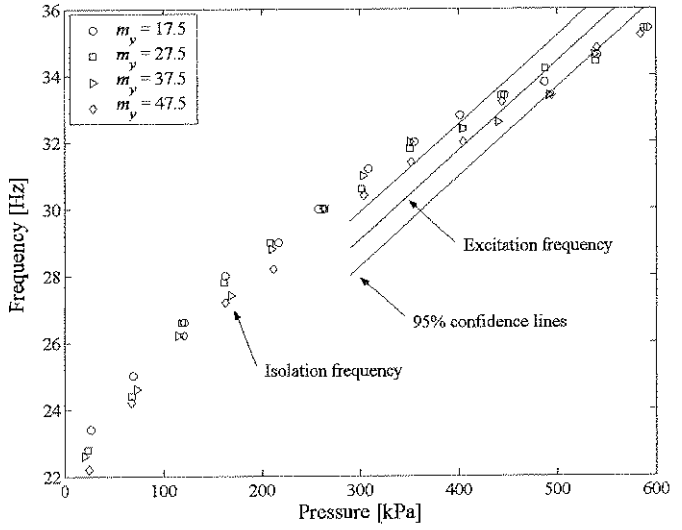

Figure 5.8: Isolation frequency *vs.* supply pressure

5.2.2 Parameter estimation

The parameters were estimated by fitting theoretical models to the experimental data. The purpose was to extract the unknown physical properties, namely stiffness and damping. Mass values were not fitted but rather measured, since this significantly improved the quality of the curve fit. The curve fit method

chosen minimised the sum of the least squares error between the predicted and measured values at each measured frequency. The value at each frequency was normalised by the sum of the squares in order to allow equal weight of values at maximum as well as minimum transmissibility. This allowed a good fit over the entire measured frequency band. The objective function used is:

$$F = \sum_{f=f_1}^{f_2} \frac{\left[|T_r'(f)| - |T_r(f)|\right]^2}{\left[|T_r'(f)| + |T_r(f)|\right]^2} \tag{5.2}$$

where T_r' is the measured transmissibility, T_r is the predicted transmissibility and f the frequency. Only the absolute values of the transmissibility were used. The standard Matlab optimisation algorithm `fmincon.m` was used to minimise the objective function. It was found that good initial values are essential for a converged solution. Several models were fitted to the measured data. Although some of the curve fits provided results that appeared valid, on closer inspection this was found not to be the case. The main problem was how to compensate for the effects of spring and membrane geometry. Initial attempts used a compensation factor for membrane size as a variable in the optimisation algorithm, but these did not provide accurate estimates of the membrane stiffness. Finally an accurate model accounting for both membrane and spring geometry was developed (refer to Appendix E). The model is shown in Figure 5.9.

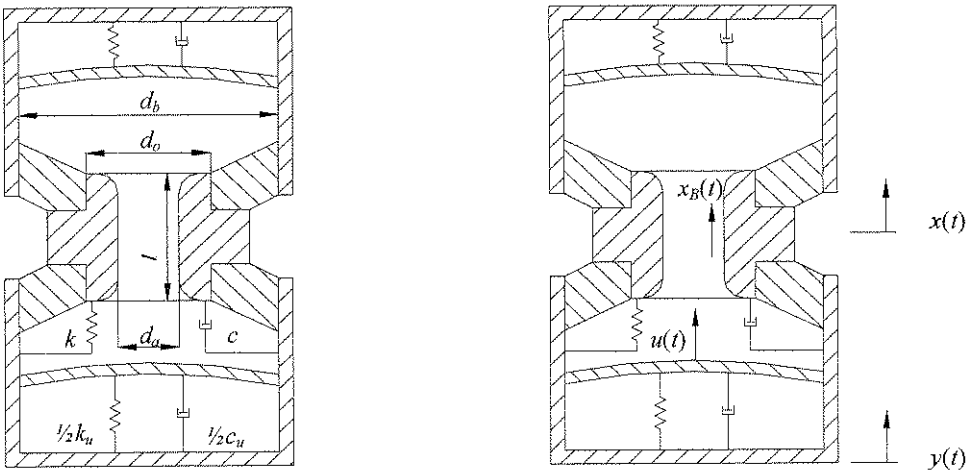

Figure 5.9: Type I AVAI model accounting for geometrical effects

The main difference in this model is that the effect of the conical primary spring geometry as well as the deformed shape of the membrane is taken into account when calculating the continuity equation [Equation (E.10)]:

$$x_B = C_1 y - C_2 x + C_3 u$$

$$\text{where: } C_1 = \frac{1}{3}\frac{A_b}{A_a}\left[\left(\frac{d_o}{d_b}\right)^2 + \frac{d_o}{d_b} + 1 - S_f\right]$$

$$C_2 = \frac{1}{3}\frac{A_b}{A_a}\left[\left(\frac{d_o}{d_b}\right)^2 + \frac{d_o}{d_b} + 1\right] - 1 \tag{5.3}$$

$$C_3 = S_f \frac{A_b}{A_a}$$

S_f is the membrane shape factor and is 1 if the membrane edge has the same displacement as its centre, ½ if its deformation approximates a paraboloid and ⅓ if a fixed (no rotation) boundary condition is assumed (Appendix E).

If excitation occurs at the x degree of freedom the transmissibility is [Equation (E.23)]:

$$\frac{Y}{X}=\frac{-\omega^2 m_B C_2 C_3\left(k_u+i\omega c_u+\omega^2 m_B C_1 C_3\right)+\left(k_u+i\omega c_u-\omega^2 m_B C_3^2\right)\left(k+i\omega c-\omega^2 m_B C_1 C_2\right)}{\left(k_u+i\omega c_u-\omega^2 m_B C_3^2\right)\left[k+k_u+i\omega\left(c+c_u\right)-\omega^2\left(m_y+m_B C_1^2\right)\right]-\left(k_u+i\omega c_u+\omega^2 m_B C_1 C_3\right)^2} \tag{5.4}$$

The constant values used in the fitting procedure are shown in Table 5.2. The values for the remaining parameters were found with the curve fit procedure. Typical curve fits for a 47.5 kg isolated mass at 585 kPa and a 17.5 kg isolated mass at 592 kPa are shown in Figure 5.10. The complete dataset was used for the curve fits resulting in a compromised fit over the frequency band. If an accurate fit of the natural frequency is required the weight for that frequency range can be increased, but this will result in lower correlation at other frequencies.

Table 5.2: Constants in curve fitting

	Variable	Value
Port diameter [m]	d_a	0.014
Reservoir diameter [m]	d_b	0.063
Spring outer diameter [m]	d_o	0.050
Isolated mass [kg]	m_y	17.5 27.5 37.5 47.5
Density [kg/m^3]	ρ	1000
Port length [m]	l	0.1
Membrane shape factor	S_f	⅓

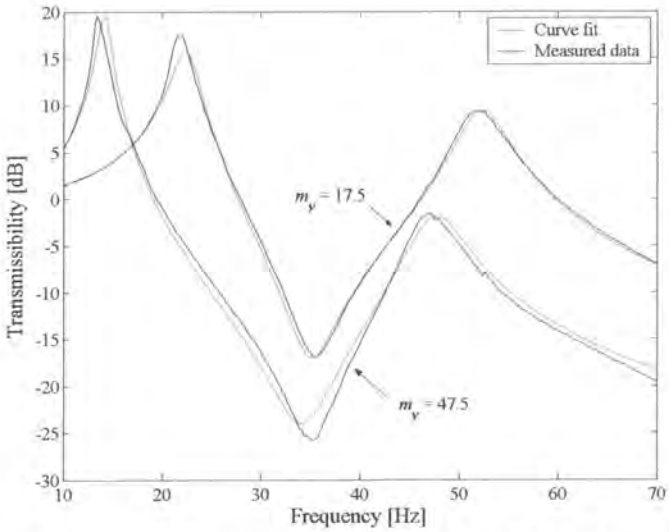

Figure 5.10: Typical curve fits for 47.5 kg at 585 kPa and 17.5 kg at 592 kPa

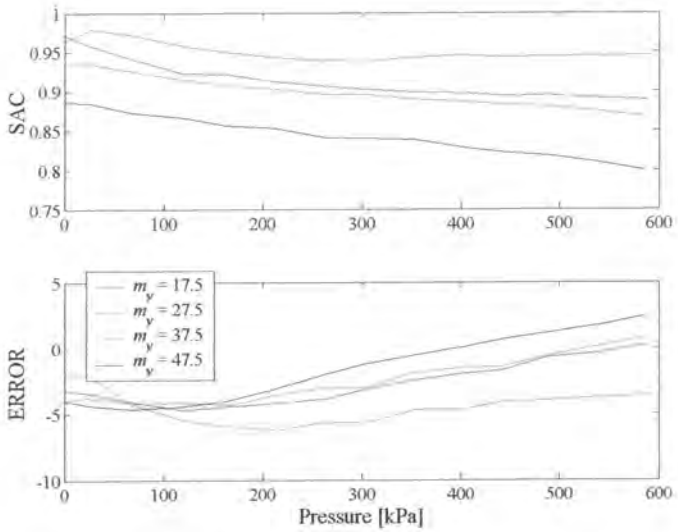

Figure 5.11: SAC and ERROR values *vs.* supply pressure

The quality of the curve fits was assessed by calculating the signature assurance criterion (SAC) and the ERROR values. These values are defined as (Dascotte & Strobbe, 1999):

$$\text{SAC} = \frac{\left|\alpha_X^H \alpha_A\right|^2}{\left(\alpha_X^H \alpha_X\right)\left(\alpha_A^H \alpha_A\right)}$$
$$\text{ERROR} = 100 \cdot \frac{\sum_{j=1}^{M} \alpha_{A_j} - \sum_{i=1}^{N} \alpha_{X_i}}{\sum_{i=1}^{N} \alpha_{X_i}} \tag{5.5}$$

α_X and α_A are the experimental and predicted transmissibilities respectively, and ^{H} denotes the Hermitian transpose. A SAC value of 1 indicates perfect correlation while the ERROR value should ideally be zero. The SAC and ERROR values are shown in Figure 5.11. The figure indicates good correlation between the model and the measured data. The correlation is better at lower isolated mass values. This can be explained by the deformation of the primary spring under static load, the effect of which can also be seen in the fitted parameter values shown in Figure 5.12. The primary system spring stiffness is a function of material property and geometry. It was observed that the geometry of the spring changes substantially due to static deflection, which explains the different values obtained. The maximum difference was 20%. The difference in values with pressure can also be explained by a change in geometry due to the pressure differential between the reservoir and atmosphere. The variation in primary system damping was less and because the damping is not expected to be a function of geometry. For the four isolated masses used the membrane stiffness was found to be similar in each case and consistently increased with pressure.

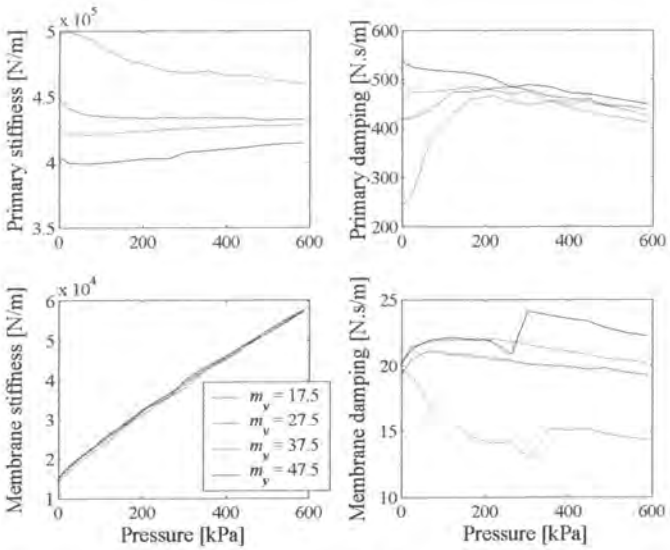

Figure 5.12: Fitted parameters

5.3 Type II AVAI

5.3.1 Experimental results

For these tests the AVAI was fitted to an Schenck hydraulic actuator. Random excitation was used and the 100 mV/g PCB ICP accelerometers were sampled with a frequency resolution of 0.156 Hz. The pressure was varied using a manual pressure regulator in increments of ~50 kPa from 0 to 519 kPa. Figure 5.13 shows the change in transmissibility as the supply pressure is increased. The envelope of these curves is shown in Figure 5.14. From this figure it is clear that the minimum transmissibility is a function of pressure. This is not predicted by the theory presented in Chapter 2 and is a result of the implementation. In contrast with the approach followed with the type I AVAI, in this case the theoretical model will not be updated to describe this effect since it is unwanted and it is believed that it will be possible to eliminate it by design. The device must therefore be changed to more closely represent the theoretical model and not the other way around. This approach will be followed in future work. Clearly there is a diminishing return in tuning since the transmissibility at the isolation frequency increases with increasing pressure.

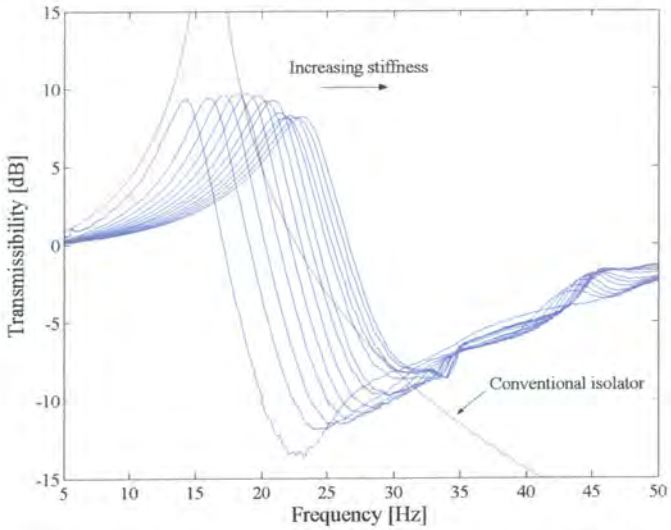

Figure 5.13: Change in transmissibility as the air spring stiffness is increased

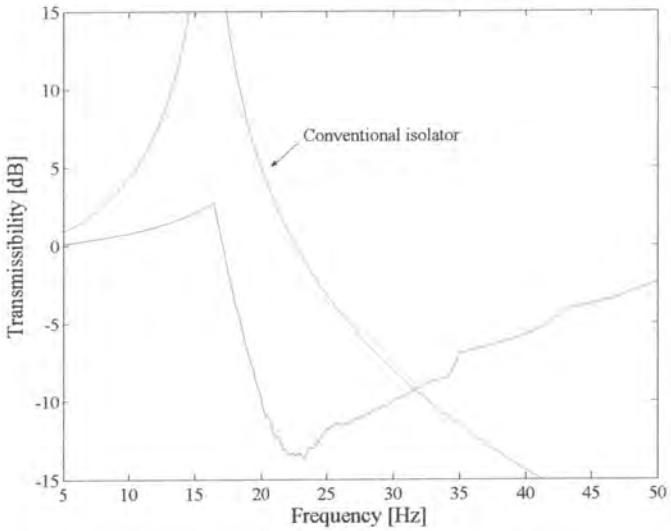

Figure 5.14: Transmissibility envelope

The isolation frequency was calculated as shown before in Figure 5.5, but in this case a 3rd degree polynomial was used since it was found to be more realistic. The relationship between isolation frequency and pressure is shown in Figure 5.15. The frequency range was between 23 at 32 Hz which is slightly too low for the pneumatic drill, but this can easily be remedied by reducing the air spring volume.

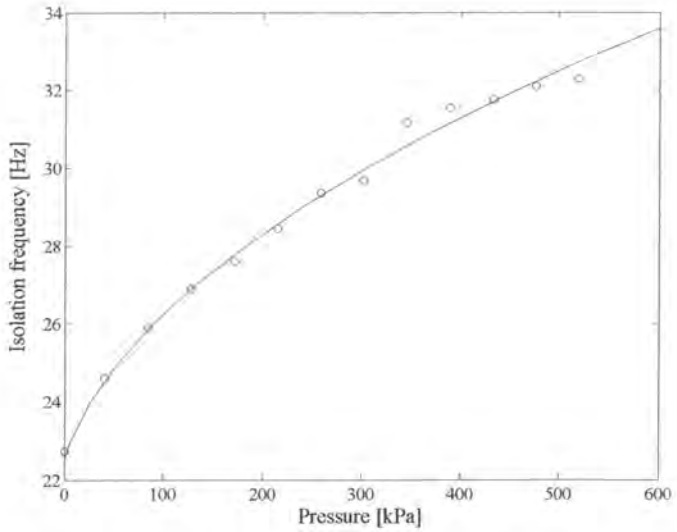

Figure 5.15: Isolation frequency *vs.* supply pressure

The supply pressure (p_s in bar) excitation frequency (f_e in Hz) relationship is:

$$p_s = 0.0371 f_e^2 - 1.5421 f_e + 15.8923 \tag{5.6}$$

It was found that the the bandwidth and robustness was not influenced by pressure as illustrated in Figure 5.16.

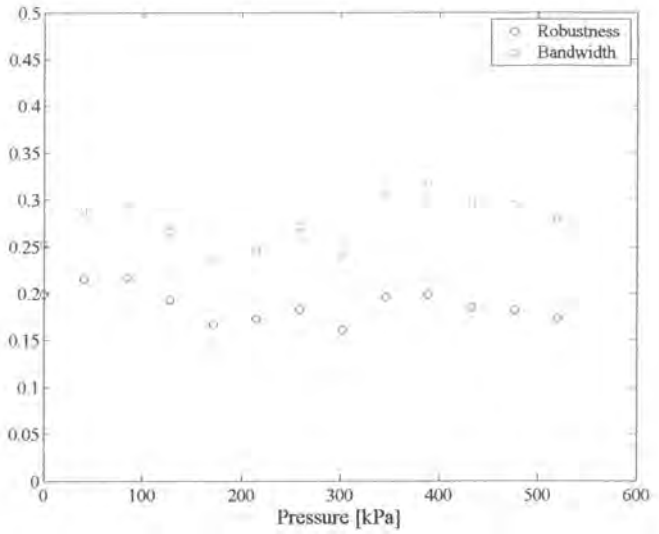

Figure 5.16: Bandwidth and robustness *vs.* supply pressure

5.3.2 Parameter estimation

The same parameter estimation procedure as for the type I AVAI was followed. In this case there are only two unknown parameters, namely the stiffness and damping. The constant values used for the curve fit are shown in Table 5.3. Again several models were fitted and it was found that some

inaccuracy is present in the area ratio estimation. The effective reservoir area ratio can be calculated as was shown in Chapter 4 by assuming a conical deformation of the membrane, while the maximum area ratio is given by reservoir area. If the area ratio varies with pressure then it will be expected to fall somewhere between these values.

Table 5.3: Constants used for curve fitting

	Variable	Value
Slug diameter [m]	d_a	0.02
Reservoir outer diameter [m]	d_b	0.05
Reservoir inner diameter [m]	d_i	0.032
Isolated mass [kg]	m	3.5
Density [kg/m^3]	ρ	14500
Slug length [m]	l_s	0.06
Effective area ratio	A_e/A_a	4.27
Maximum area ratio	A_b/A_a	6.25

A typical curve fit for various area ratios is shown in Figure 5.17. The red curve is the result when the area ratio is treated as a variable in the optimisation process. Normally one would not consider the area ratio to be variable, but due to the construction of the type II AVAI it is possible that small variations in area ratio can exist. This is due to air trapped in the reservoir region that will have an influence on continuity at low air spring pressures.

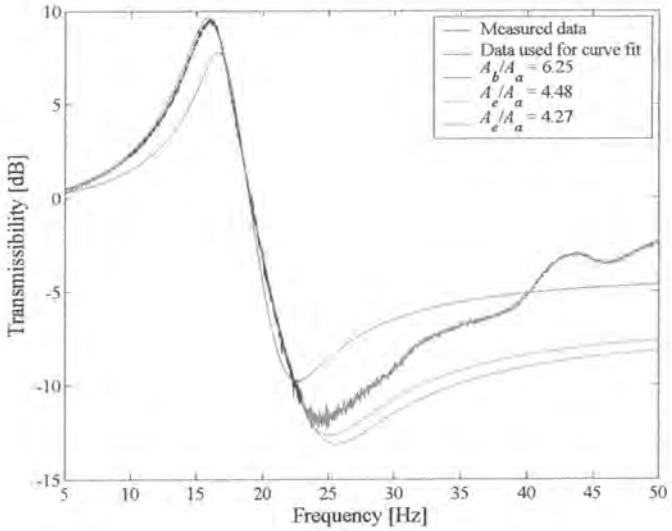

Figure 5.17: Curve fit comparison at 41 kPa

The fitted parameter results are shown in Figure 5.18. The stiffness was changed 3.6 times from 72 to 265 kN/m. At the normal operating pressure of the rock drill the stiffness is 187 kN/m, which is more than adequate since it resulted in a static deflection of 1.6 mm at 30 kg of force. The damping ratio is fairly constant at ~0.1, which is low, as would be expected from an air spring. The maximum difference between the calculated and effective area ratios is 30%. The area ratio remains a concern since it has a large influence on the design while it turned out to be difficult to estimate accurately. In future designs it should be considered to remove this uncertainty by using an additional convolution in

the bellow in the reservoir region. For such a case the area ratio is the average of the inner and outer diameters. The air trapped in the reservoir region should also be limited. Although attempts have been made to minimise any trapped air, additional measures such as pressurising the reservoir can be considered.

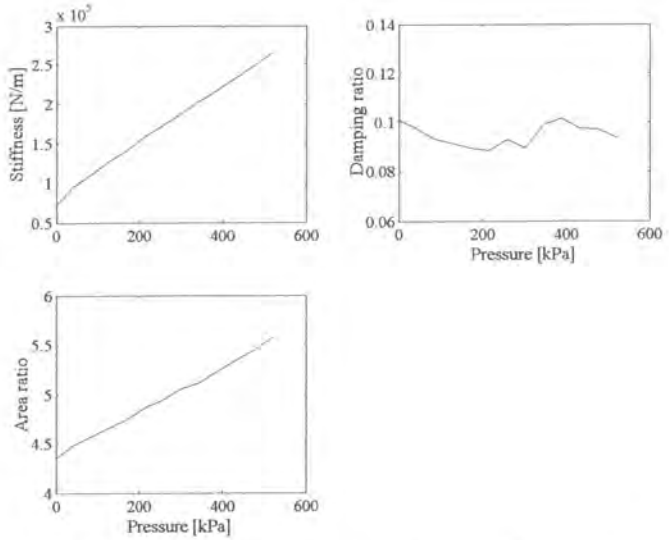

Figure 5.18: Fitted values for stiffness, damping and area ratio *vs.* supply pressure

The quality of the curve fits is not as good as for the type I AVAI as shown by the SAC and ERROR values in Figure 5.19. These values confirm that the variable area ratio fit is more accurate and therefore the parameters for stiffness and damping ratio for this model are believed to be more precise (Figure 5.18).

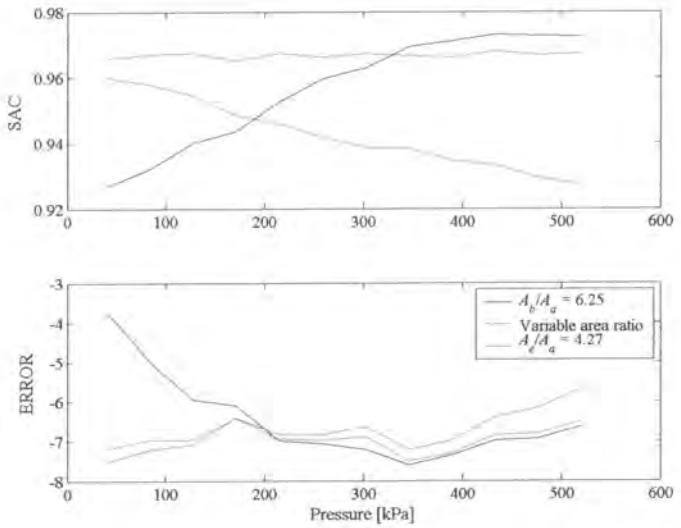

Figure 5.19: SAC and ERROR values *vs.* supply pressure

5.4 Control

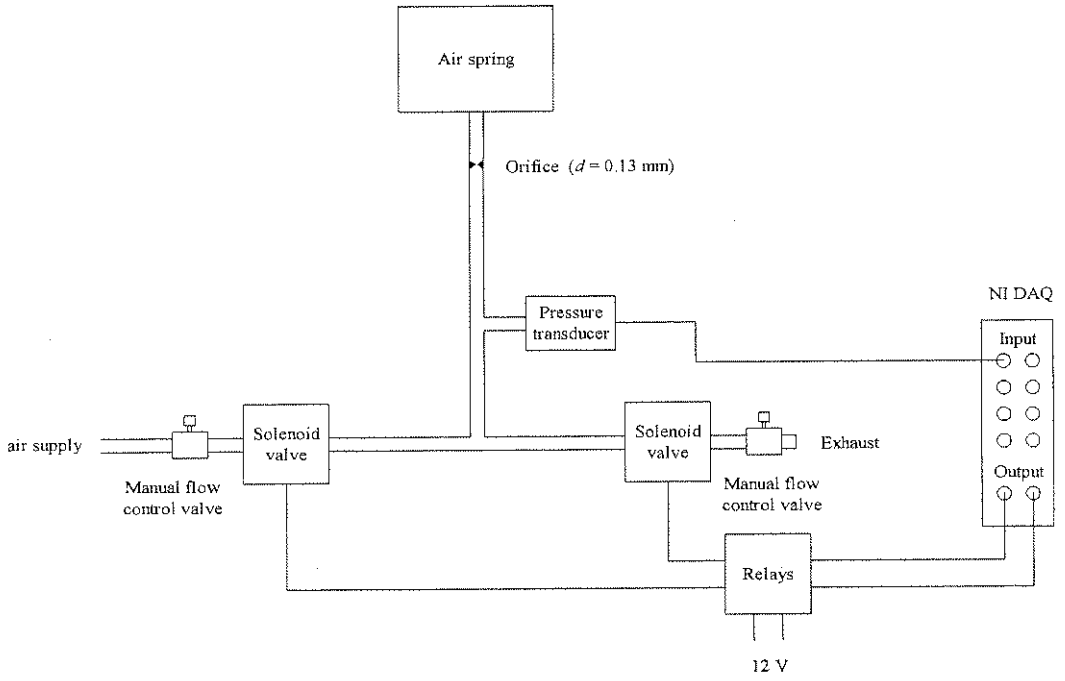

Figure 5.20: Pressure control valve

To demonstrate that the AVAI can be controlled to minimise the transmission of varying tonal excitation, the experimental set-up of Figure 5.1 was modified such that the manual pressure regulator was replaced by electronically controlled solenoid valves as shown in Figure 5.20. Although electronic pressure regulators are available as standard items from pneumatic equipment suppliers, it was decided to build one using components that were readily available. The advantage of this decision was cost effectiveness, but the time needed to change the pressure was significantly longer. Since the objective of this experiment was to show that the control method works and not the speed at which it could change the isolation frequency, the valve system was considered adequate.

The operation of the control system for the supply pressure is explained in Figure 5.20. The National Instruments 6024E DAQ card was nsed to open the appropriate valve and sample the pressure transducer simultaneously. The pressure transducer is located in the supply line before the orifice and not inside the airspring. This location is necessary to make sure that the pressure fluctuation in the airspring, as it is compressed, does not inflnence the measurements. The fluctuation in the supply line due to the air spring operation will of course be a lot less because of the orifice. Once the pressure reached the command pressure within adeqnate accuracy, the valve was closed. After the valve is closed leak-flow will occur to or from the air spring through the orifice resulting in the pressure changing to a value outside the specified tolerance. To make sure that the command pressure is reached the pressure is sampled again after a short delay and reset if necessary. This procedure continued until the pressure stabilised. In practice the pressure was set after ~5 attempts. The pressure set procedure is explained in the flow diagram shown in Figure 5.21.

A practical aspect to consider when setting the pressure is the case where the optimisation algorithm calculates a pressure that cannot be obtained physically. If, for instance, a pressure of 700 kPa is computed, the pressure set algorithm will be sent into an endless loop since the supply pressure is only 600 kPa. This can, of course, be remedied easily by using a constraint on the maximum stiffness, hut even here caution is necessary. If, for instance, the algorithm uses a penalty function approach it could calculate a stiffness value outside the achievable range. Another such case occurs when a finite difference calculation tries to use an out-of-range stiffness value to calculate the derivative. The above issues are particular to the algorithm used and each design must therefore be carefully studied to ensure safe operation under all conditions.

Only the type I AVAI was used to demonstrate the controllability. The standard Matlab optimisation algorithm `fmincon.m` was used for this purpose. This function is an implementation of the sequential quadratic programming (SQP) optimisation algorithm and can handle constraints. Since it is assumed that the excitation is tonal, it is possible to calculate the transmissibility in the time domain by simply dividing the rms output by the rms input value of a short set of sampled values, as was explained in Chapter 3. It would be possible to minimise the rms output only, but that would not take account of varying input amplitude. The objective function used is:

$$f(p) = \frac{\frac{1}{T}\sum_{i=1}^{N} \ddot{y}_i^2}{\frac{1}{T}\sum_{i=1}^{N} \ddot{x}_i^2} \tag{5.7}$$

where $\ddot{x}$ is the input and $\ddot{y}$ the output acceleration.

The excitation frequency can be estimated using zero-crossings, which is a fast and effective technique for tonal signals. Using an FFT can also be considered, but it does have some disadvantages, notably the time required for an accurate estimate. For this experiment the mean period of a number of zero-crossings was used to calculate the excitation frequency. To make sure that the measured signal does not contain frequencies other than the excitation frequency, a 6^{th} order Butterworth band-pass filter was applied before the estimation process.

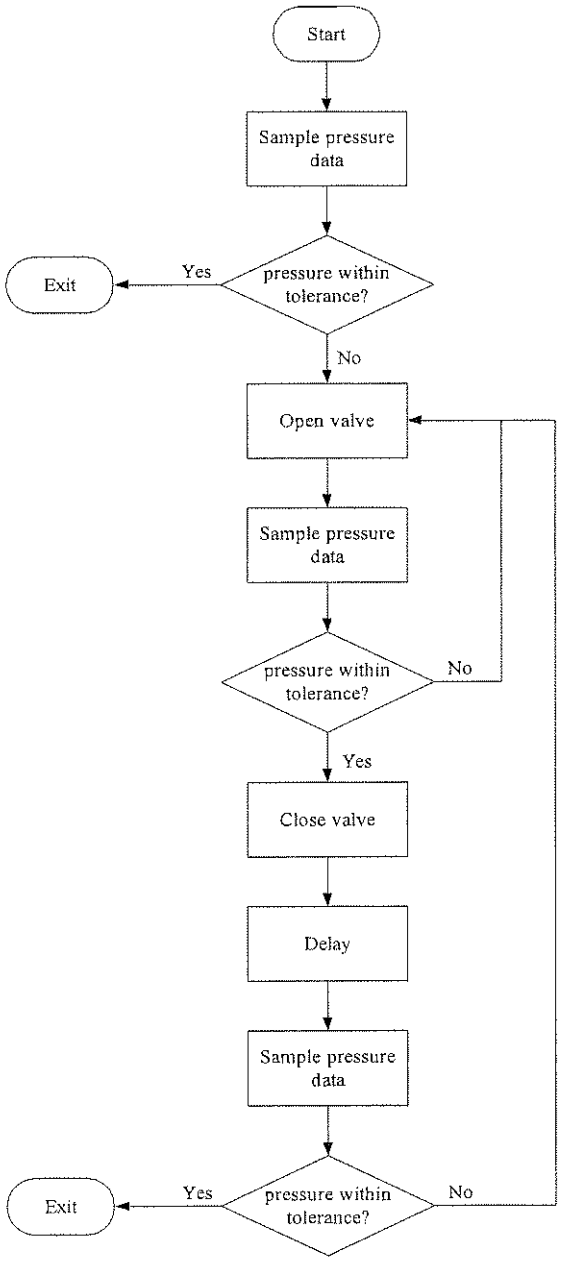

Figure 5.21: Pressure set flow diagram

The flow diagram of the control process is shown in Figure 5.22. Initially the device is tuned using the isolation frequency obtained from the characterisation test. After the pressure is set using this open loop technique, the optimisation algorithm is started in an attempt to find a better solution. The excitation frequency is calculated for each measurement of the objective function and if a change of more than 10% is observed the optimisation problem is restarted. For a practical system the change in excitation frequency allowed will be set according to the system bandwidth and the expected rate of change in excitation frequency. In the control process a constraint on the stiffness value was calculated to ensure that a too low stiffness does not make convergence impossible. The need for the constraint

was discussed in Chapter 3. The experimental 2nd frequency of maximum transmissibility value calculated from the characterisation test was used as the constraint:

$$\hat{p}_s = 0.66 f_e^2 - 22.03 f_e + 135.42 \tag{5.8}$$

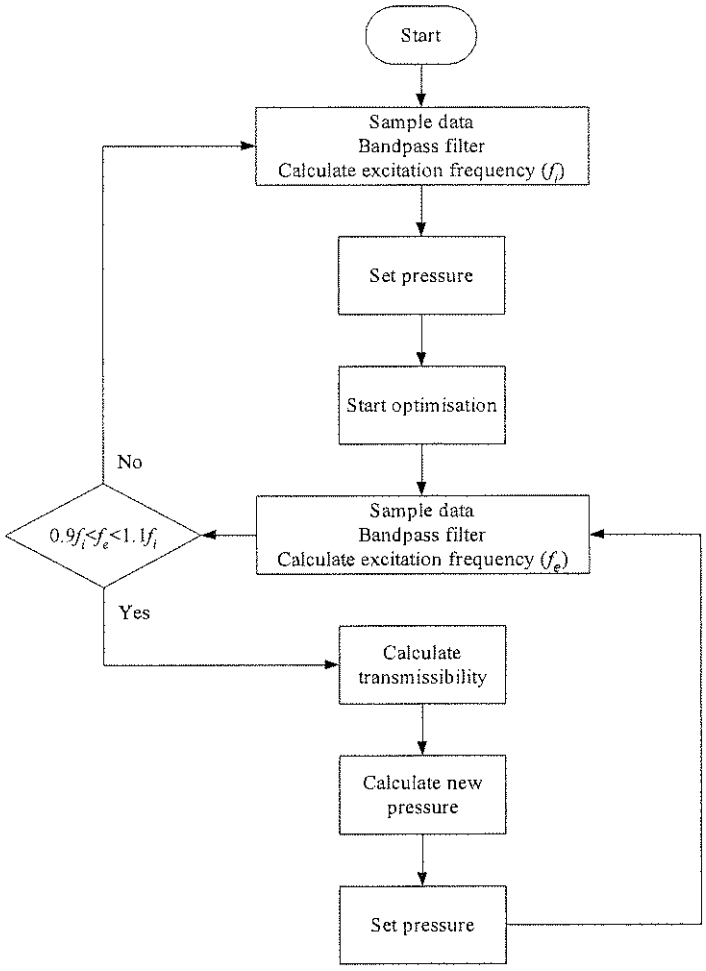

Figure 5.22: Control flow diagram

The results for a frequency step from 30 to 35 Hz are shown in Figure 5.23. The result is only used to illustrate that the method can work and was not fine-tuned to give the best result possible. All the issues regarding different algorithms were discussed in Chapter 3 and the advice contained therein should be followed when a control system is designed for the AVAI.

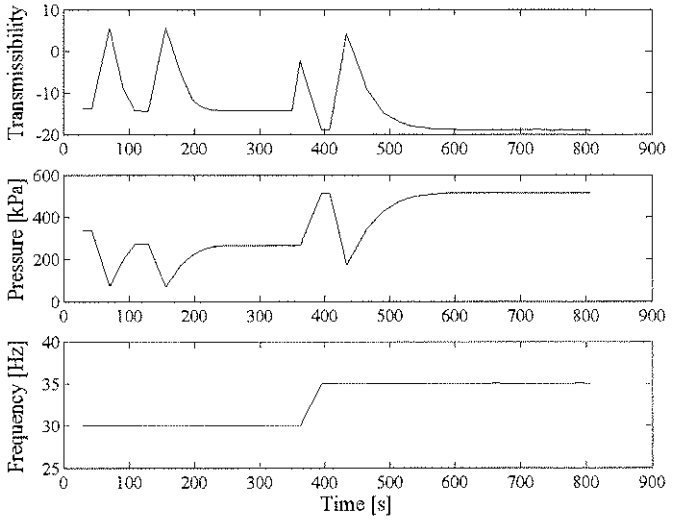

Figure 5.23: Control result when changing the excitation frequency from 30 to 35 Hz

5.5 Conclusion

This chapter verified the mathematical models used for the two AVAIs by using experiments. In both cases the effects seen in experiments were not fully explained in the initial mathematical models and these had to be modified. The modified models represent a reasonable estimate of the actual system behaviour and can be used to design the AVAIs. Due to various practical aspects it will not be possible to eliminate testing entirely and some tuning would still be required for new designs. It is, however, believed that the models suggested will minimise the amount of modification needed after such testing.

This chapter also confirmed experimentally that the system could be controlled successfully. Control was only implemented for the type I AVAI so as to demonstrate the method. The experiment sbowed that it is possible to detect a step change in frequency and that the device can successfully be tuned to the new excitation frequency.

6 Conclusions

The ideal isolator is one that will support the equipment being isolated without transmitting any dynamic forces. An isolator with infinite static stiffness and zero dynamic stiffness will achieve this goal. Although this ideal isolation cannot be obtained in practice, it can be approximated through a wide range of devices. The approximation occurs over a limited frequency band and methods of increasing this band were investigated. The methods were classified as passive, adaptive and active techniques. Passive techniques offer no flexibility, while active techniques approach optimal isolation performance. Adaptive techniques can be seen as a compromise of flexibility and cost.

The isolation philosophy introduced the concept of adapting the isolator properties by considering both the input characteristics and a set of evaluation criteria. The criteria could typically be represented by a filter that would weigh the frequencies according to their importance. An optimisation technique can then be applied to find the optimal set of isolator parameters that will minimise the criteria. The system functions on-line in such a way that near optimal performance can be guaranteed as the input or isolator characteristics vary with time.

Chapter 1 compared a wide range of isolators concepts, starting at the most simple passive isolator and ending with the active amplified vibration-absorbing isolator. To compare the various devices the non-dimensional blocked transfer dynamic stiffness was defined. This quantity was found to represent the isolator properties without the additional complication of the equipment being isolated, as happens in traditional transmissibility methods. Some isolation methods cannot be explained by considering the dynamic stiffness alone and only in those cases were the transmissibility calculated. Methods used to improve vibration absorbers were adapted to isolators with interesting results, which can be investigated in future work. The focus of this work was the broadening of the effective low stiffness bandwidth of the amplified vibration-absorbing isolator by adapting system parameters. A sensitivity study showed that the isolation frequency is the most sensitive to geometric variables, but these cannot be changed easily in practice. A considerable amount of work has been published on variable stiffness devices. The range of stiffness values that can be attained and the speed at which it can be realised remains a problem.

In chapter 2 time and frequency-domain methods were used to study two novel adaptive amplified vibration-absorbing isolators. The type I AVAI used flexible reservoir walls to adapt the isolation frequency. The type II device incorporated a heavy metal slug. Both devices used variable pressure air springs to change the stiffness. The use of air springs was convenient, offered low damping and had the ability to be used with the pneumatic rock drill to eliminate the need for a control system. Conceptual design methodologies were illustrated for both damped and undamped fixed and adaptive isolation frequency AVAIs. To determine the effects of tuning, the equations were transformed in terms of constant frequency ratios and the stiffness ratio. The stiffness ratio was the only tuning parameter considered.

To design the type I AVAI for fixed frequency excitation, optimisation was employed. This approach made it possible to set goals for the required bandwidth and the proximity of the frequencies of

maximum transmissibility to the isolation frequency. For the adaptive AVAI it was shown that specific choice of the area and mass ratios could influence the tuning range. For the damped adaptive AVAI the transmissibility at the isolation frequency was minimised when the area ratio was minimised and the mass ratio maximised. This AVAI had a constant static deflection, which could be advantageous in practice.

For the type II AVAI the main spring stiffness was made adaptive. The design methodology is different from the type I because the travel of the slug is restricted and must enter the design process to ensure that realistic area ratios are chosen. A design methodology was proposed that starts with the overall device size and calculates the port diameter required. It was shown that a maximum of two solutions could exist for each specified set of outside dimensions. Three additional models were analysed each considering specific refinements to the basic model. The first investigated the effect of rubber stops as an alternative to slug springs as a method for keeping the slug centred vertically. The second took account of leakage between the port and the slug, which was shown to increase the isolation frequency. It was concluded that the gap should be minimised. The third showed the effect of using rolling diaphragm seals to eliminate leakage. The rolling diaphragm seal will result in a larger device since the effective mass is reduced.

Chapter 3 showed how optimisation could be used as a control method for the AVAI. Several objective functions were investigated including a ratio of output to input rms acceleration, quadrature of the input and output accelerations and the H_1 transmissibility estimator. Quadrature can only be used if the damping is small, while the rms method will be easy to implement for a damped device. The H1 estimator was considered to be the most accurate. Four separate scenarios were considered. The first case assumed that the device needed to be tuned at start-up only. It was shown that as long as the initial condition is appropriate and the step size can be controlled, the device could be tuned successfully. For the type I device the initial condition had to be the maximum stiffness ratio that could be achieved, while for the type II it must he the minimum. The second case considered a sudden change in excitation frequency. For this case it was found that standard algorithms would not be successful. The lfopc algorithm could be used in this case. The third case considered a slow change in either the excitation frequency or the system properties. Due to incorrect gradient information this case cannot be handled using the optimisation method. Lastly, a general method was proposed where open-loop tuning was used as a first stage and optimisation as fine-tuning during a second stage. The open-loop tuning is done using a look-up table established from a characterisation test. The look-up table is updated with the information from the subsequent optimisation procedure if a lower transmissibility is found. This method will be fast and will maintain its accuracy over time.

Chapter 4 showed how the design of an AVAI could be applied to a practical isolation problem. Pneumatic rock drills are commonly used in the South African gold mining industry. It has been found that the operators of these drills are exposed to harmful vibration levels. The maximum weighted equivalent acceleration value measured on these drills at a test facility was 18.72 m/s^2. The excitation of these drills has a large tonal component, but also consists of wide-band noise. The tonal component contributes ~50% to the overall weighted equivalent acceleration and any isolation method must therefore address it with care. Measurements showed that the frequency of the tonal component is a function of supply air pressure. It was shown theoretically that both the AVAIs considered would have a lower weighted acceleration that an equivalent isolator, depending on the amount of damping

included. Subsequently, a simulation of the actual system behaviour showed that both AVAIs would reduce the handle response. Three tuning methods were compared. The first used the supply line pressure only, the second calculated the excitation frequency and tuned the device accordingly, while the third adapted both stiffness and damping to minimise the weighted equivalent acceleration. The last method resulted in the best performance, but using the supply line was adequate and has a major cost advantage. The type II AVAI acceleration levels were reduced to below 10 m/s^2 up to a pressure of 500 kPa for three of the drills simulated.

In chapter 5 the mathematical models used for the two AVAIs were verified using experiments. In both cases the effects seen in experiments were not fully explained in the initial mathematical models and these had to be modified. The modified models represent a reasonable estimate of the actual system behaviour and can be used to design the AVAIs. Due to various practical aspects it will not be possible to eliminate testing entirely and some tuning would still be required for new designs. It is, however, believed that the models suggested will minimise the amount of modification needed after such testing.

This chapter also confirmed experimentally that the system can be controlled successfully. Control was only implemented for the type I AVAI so as to demonstrate the method. The experiment showed that a step change in frequency could be detected and that the device could successfully be tuned to the new excitation frequency.

Future work on vibration-absorbing isolators:

1. The two AVAIs that were proposed in this work should be made more robust and must be tested on an actual pneumatic drill at the amplitudes experienced in practice.
2. The augmentation of the AVAIs to reduce the response at resonance must be investigated. This should include the addition of "skyhook" dampers etc.
3. The characteristics of the springs should be investigated so that stiffness and damping values can be predicted with greater accuracy.
4. The reduction of damping at all possible sources and under all loading conditions must be explored.

The innovative use of vibration absorbers as isolators shows promise for solving the more demanding isolation problems that exist today in a cost effective manner.